



CANCER THERAPY

Repurposing colforsin daropate to treat MYC-driven high-grade serous ovarian carcinomas

Matthew J. Knarr¹, Jamie Moon², Priyanka Rawat¹, Analisa DiFeo^{3,4}, David S. B. Hoon², Ronny Drapkin^{1,5*}

Copyright © 2024 the Authors, some rights reserved; exclusive licensee American Association for the Advancement of Science. No claim to original U.S. Government Works

High-grade serous ovarian cancer (HGSOC) is one of the deadliest cancers for women, with a low survival rate, no early detection biomarkers, a high rate of recurrence, and few therapeutic options. Forskolin, an activator of cyclic AMP signaling, has several anticancer activities, including against HGSOC, but has limited use *in vivo*. Its water-soluble derivative, colforsin daropate, has the same mechanism of action as forskolin and is used to treat acute heart failure. Here, we investigated the potential of colforsin daropate as a treatment for HGSOC. We found that colforsin daropate induced cell cycle arrest and apoptosis in cultured HGSOC cells and spheroids but had negligible cytotoxicity in immortalized, nontumorigenic fallopian tube secretory cells and ovarian surface epithelial cells. Colforsin daropate also prevented HGSOC cells from invading ovarian surface epithelial cell layers in culture. *In vivo*, colforsin daropate reduced tumor growth, synergized with cisplatin (a standard chemotherapy in ovarian cancer care), and improved host survival in subcutaneous and intraperitoneal xenograft models. These antitumor effects of colforsin daropate were mediated in part by its reduction in the abundance and transcriptional activity of the oncoprotein c-MYC, which is often increased in HGSOC. Our findings demonstrate that colforsin daropate may be a promising therapeutic that could be combined with conventional therapies to treat HGSOC.

INTRODUCTION

Ovarian cancer is currently the second deadliest gynecological malignancy worldwide and is increasing in incidence and mortality, with well over 300,000 new cases and more than 200,000 deaths as of the latest statistics (1). Epithelial high-grade serous ovarian carcinoma (HGSOC) is the most common and deadly subtype of ovarian cancer, accounting for approximately 70% of cases diagnosed and 75% of ovarian cancer deaths (2–4). Its high mortality rate is due to the absence of early symptoms, resulting in 80% of patients being diagnosed at later stages often after metastatic progression throughout the peritoneal cavity. Around 80% of tumors or metastases will recur within 5 years despite initially responding to standard platinum/taxane therapy. Patients with recurrent and chemoresistant tumors have limited treatment options. Currently, the only adjuvant therapies that are approved by the US Food and Drug Administration (FDA) and are regularly used for HGSOC treatment are poly(adenosine diphosphate–ribose) polymerase (PARP) inhibitors [which generally only benefit the subpopulation of patients with well-defined defects in DNA damage response (DDR) pathways, such as *BRCA1/2* mutation] and antiangiogenic therapy (which produces improvements in progression-free survival but not overall survival) (5–12). Thus, there is a critical need for therapies that can limit recurrence and improve survival outcomes.

Forskolin, the well-established small-molecule activator of intracellular cyclic adenosine monophosphate (cAMP) signaling, has been shown to have a variety of clinical uses, including the treatment of

cancer (13). Forskolin is a labdane diterpene derived from the roots of the Indian *Coleus forskohlii* plant, an Ayurvedic herbal medicine long used to treat a variety of disorders, such as angina, hypertension, and asthma (14–16). The canonical function of forskolin is to act as a potent, reversible stimulator of adenylyl cyclase (AC) through direct interaction with the AC catalytic subunit. This generates a rapid increase in intracellular cAMP levels and activates cAMP signaling pathways through effector proteins, such as cAMP-dependent protein kinase (PKA) and exchange protein directly activated by cAMP (EPAC) (16–18). cAMP acts as a second messenger and binds to the regulatory subunits of PKA, causing the release of the catalytic PKA subunits, which can then phosphorylate downstream targets that include cAMP response element-binding protein (CREB) (19). Phosphorylated CREB then translocates into the nucleus and binds to cAMP response elements to activate gene expression programs (20). EPAC is also activated by direct binding of cAMP and facilitates signaling changes involved in cell adhesion and proliferation (21).

With respect to cancer, forskolin can have several antitumor effects (typically through canonical activation of cAMP signaling), such as inhibition of cell growth and induction of cell death in gastric, lymphoid, and colon cancers (22–24). Forskolin has also been shown to inhibit cell migration and invasion and metastatic colonization by multiple cancer types (25–28). In addition, combination therapy of forskolin with other anticancer drugs has been shown to be synergistic in treating chemoresistant colon cancer cells in culture (24). Finally, evidence has also emerged that forskolin may be a valuable tool for targeting tumor-initiating cells by causing mesenchymal, stem-like cancer cells to transition into less aggressive epithelial-differentiated states (29). The effects of forskolin on ovarian cancer biology remain poorly defined, and only a few studies have examined the direct effects of forskolin treatment on ovarian cancer cells. Mann *et al.* have reported that combination treatment of forskolin with cisplatin (Cis) enhanced Cis accumulation within ovarian cancer cells (30), but other studies have reported that forskolin treatment was inhibitory (31). Forskolin stimulation of cAMP

¹Penn Ovarian Cancer Research Center, Department of Obstetrics and Gynecology, University of Pennsylvania Perelman School of Medicine, Philadelphia, PA 19104, USA. ²Department of Translational Molecular Medicine, Saint John's Cancer Institute, Providence Health Services, Santa Monica, CA 90404, USA. ³Department of Pathology, University of Michigan, Ann Arbor, MI 48109, USA. ⁴Department of Obstetrics and Gynecology, University of Michigan, Ann Arbor, MI 48109, USA. ⁵Basser Center for BRCA, Abramson Cancer Center, University of Pennsylvania School of Medicine, Philadelphia, PA 19104, USA.

*Corresponding author. Email: rdrapkin@penncmedicine.upenn.edu

signaling has been reported to cause phosphorylation of claudin-3 to alter tight junctions and stimulate production of granulins-epithelin precursor (GEP) in ovarian cancer cells (32, 33). However, these studies did not examine whether forskolin caused any phenotypic changes in the ovarian cancer cells. An additional study by Warrenfeltz and colleagues showed that forskolin treatment could inhibit the migration of SKOV3 cells in culture (31). There are conflicting reports as to whether cAMP signaling itself is pro- or antitumorigenic with respect to ovarian cancer. However, most of the data in the literature support an antitumorigenic role for activated cAMP signaling through mechanisms that include decreased proliferation, increased senescence, and increased chemosensitivity (34–40).

These studies provide a strong rationale for investigating whether forskolin could be used for HGSOc treatment. Forskolin has been used in the clinic for the treatment of glaucoma and is being investigated for the treatment of asthma, heart failure, and obesity (41–46). However, forskolin is sparingly soluble in aqueous solution and is nonideal for translation to the clinic. A water-soluble derivative, colforsin daropate (NKH 477, abbreviated here as CF), has been previously synthesized and shown to have similar biological effects (47). CF has also been used in the clinical setting for the treatment of heart failure, cerebral vasospasm, and cardiac inflammation (48–50). The combination of favorable pharmacokinetic properties and low reported toxicity makes CF an ideal candidate for drug repurposing. Here, we investigated whether CF can be used for the treatment of HGSOc. We found that it has the potential to be HGSOc cell selective, mechanistically targeting those with up-regulated MYC signaling. It was effective in HGSOc cells that were resistant to a standard ovarian cancer chemotherapeutic and synergized in those that were sensitive. Overall, this study shows that CF should be further explored for the treatment of MYC-abundant HGSOc.

RESULTS

CF induces ovarian cancer cell cycle arrest and cell death

To begin investigating whether CF had potential as a cancer therapeutic, we treated a panel of established HGSOc cell lines (Fig. 1A) with CF in culture and assessed for cytotoxic effects. Cell viability was reduced in the HGSOc cell lines with an increasing dose of CF but with a range of sensitivities among the cell lines, with the half-maximal inhibitory concentration (IC_{50}) values ranging from approximately 0.5 to 40 μ M (Fig. 1A). Given the translational potential of CF, we also treated two sets of isogenic Cis-sensitive and Cis-resistant HGSOc patient-derived xenograft (PDX) cell lines: OV81.2 and OV231 (sensitive) and OV81.2 CP40 and OV231 CP30 (resistant) (51). We confirmed the Cis resistance of the latter cell lines (fig. S1A) and observed that all four PDX cell lines were sensitive to CF, with IC_{50} values between 10 and 15 μ M; the IC_{50} values of the Cis-resistant cells were not significantly different from those of the Cis-sensitive cells (Fig. 1B). These data suggested that CF was effective at killing HGSOc cells in both Cis-resistant and Cis-sensitive contexts. To determine whether the cytotoxic effects were selective to cancer cells, we also included a panel of immortalized, nontumorigenic cell lines [human fibroblasts, fallopian tube secretory epithelial cells (FTSECs), and ovarian surface epithelial (OSE) cells] (Fig. 1C). We observed that the HGSOc cell lines were more sensitive to CF than the nontumorigenic cells (IC_{50} , approximately 1 to 40 μ M), which included FTSECs and IMR90 fibroblasts (IC_{50} , approximately 110 to >500 μ M) (Fig. 1C). On the basis of the cell viability response of the

HGSOc panel to CF, we selected HEYA8, OVCAR8, and OVCAR4 cells to model sensitive, intermediate, and resistant CF responses, respectively, in subsequent experiments. Next, we investigated the effects of CF on low-density cell survival and colony formation using a clonogenic assay (Fig. 1D). We observed a similar pattern of survival inhibition and reduced growth in the results of the clonogenic assays, with HEYA8 being the most sensitive and the two OVCAR cell lines being more resistant (Fig. 1D). It was also observed that the decreases in survival and clonogenic growth were again selective for HGSOc cells over FTSEC cells (Fig. 1, D and E).

After the observation that CF reduced proliferation and colony formation of HGSOc cells, we next wanted to determine whether the specific mechanism was increased cell death, cell cycle arrest, or a combination of both. To answer these questions, we treated our panel of HGSOc and FTSEC cell lines with increasing doses of CF and performed annexin V/propidium iodide (PI) staining of live cells to assess changes in apoptosis and PI staining of fixed cells to assess changes in cell cycle populations. In general, we found that CF decreased cell proliferation through a combination of increased cell cycle arrest and increased apoptotic cell death (Fig. 1F and fig. S1, B and C). For the FT240 cells, substantial changes in cell death and cell cycle arrest only occurred at the highest dose tested (fig. S1, B and C). HEYA8 cells had significant increases in apoptosis and G_2 -M arrest starting at doses of 1 μ M. OVCAR8 cells displayed a different pattern, with most of the cells accumulating in G_2 -M but with less apoptosis. OVCAR4 cells showed significant accumulation in the >4N or aneuploid subpopulation and did not show increased apoptosis (Fig. 1F). In addition to the experiments performed with CF, we also assessed the antitumorigenic properties of the parent compound forskolin. We observed comparable decreases in cell viability, increased cell death, and cell cycle arrest of HGSOc cells treated with forskolin (fig. S2, A to D). These data indicated that both compounds produced the same phenotypic response in HGSOc cells and that the cytotoxic effects were not selective to CF. Together, these data show that HGSOc cells in general are more sensitive to the cytotoxic effects of CF versus nontransformed FTSEC cell lines, Cis-resistant HGSOc cells remain sensitive to CF, and CF cytotoxicity occurs through a combination of cell cycle arrest and cell death.

Growth of ovarian cancer spheroids is inhibited by CF

Given that ovarian cancer cells tend to metastasize as drug-resistant spheroids, we also wanted to determine whether CF could cause cell cycle arrest and/or cell death in HGSOc spheroids (52, 53). To investigate the effects of CF on ovarian cancer spheroids, we cultured our panel of HGSOc cell lines under ultralow attachment (ULA) conditions in medium containing increasing doses of CF. We observed that CF was able to inhibit HGSOc spheroid growth in a dose-dependent manner (Fig. 2, A and B). We observed a similar pattern of sensitivity with HEYA8, OVCAR8, and OVCAR4 cells, going from most to least sensitive, respectively (Fig. 2, A and B). Analysis of apoptosis and cell cycle for the spheroids after CF treatment showed that HEYA8 cells responded predominantly with G_1 cell cycle accumulation along with apoptosis at higher doses (Fig. 2, C and D, and fig. S3, A and B). OVCAR8 cells responded with increases in apoptotic populations and 10 to 20% G_2 -M accumulation at high doses (Fig. 2, C and D, and fig. S3, A and B). OVCAR4 cells had a predominant change in cell cycle with increased aneuploid accumulation and increases in early apoptosis (Fig. 2, C and D, and fig. S3, A and B). The ability of HGSOc cells to adhere to each other

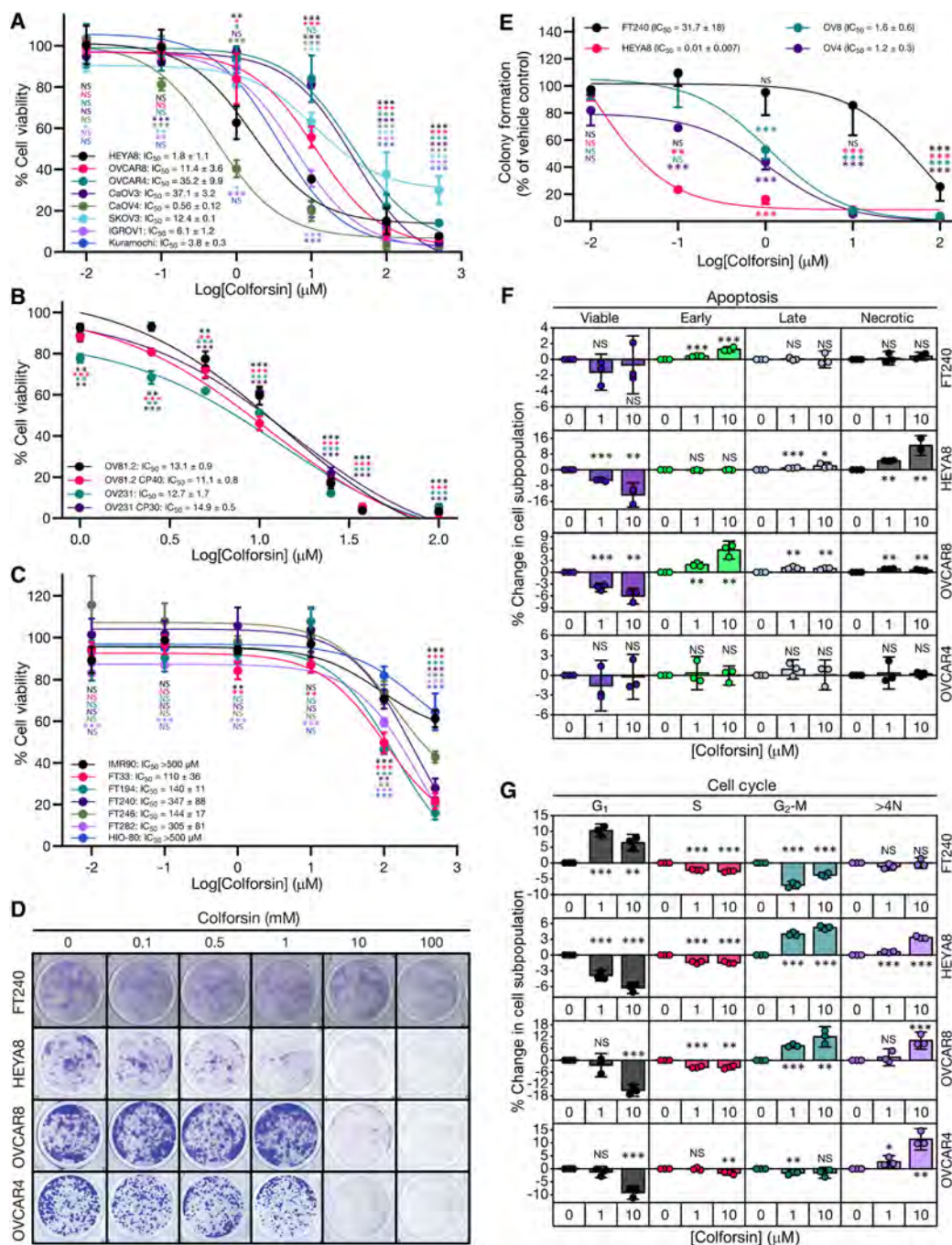


Fig. 1. CF induces cell cycle arrest and cell death in ovarian cancer cell lines. (A) Graph of dose-response curves for MTT cell viability assays of HGSOV cell lines treated with CF for 48 hours. All statistical comparisons are between a given CF dose versus vehicle control within each cell line. Mean IC_{50} values \pm SD are shown for each cell line in the legend. (B) Graph of dose-response curves for MTT cell viability assays of HGSOV PDX cell lines treated with CF for 48 hours. All statistical comparisons are between a given CF dose versus vehicle control within each cell line. Mean IC_{50} values \pm SD are shown for each cell line in the legend. (C) Graph of dose-response curves for MTT cell viability assays of nontumorigenic FTSEC, HIO-80, and fibroblast IMR90 cell lines treated with CF for 48 hours. All statistical comparisons are between a given CF dose versus vehicle control within each cell line. Mean IC_{50} values \pm SD are shown for each cell line in the legend. (D) Representative images of day 7 clonogenic survival assays for FTSEC and ovarian cancer cell lines treated with increasing doses of CF. (E) Graph depicting dose-response curves for clonogenic assays of FTSEC and ovarian cancer cell lines. All statistical comparisons are between a given CF dose versus vehicle control within each cell line. Mean IC_{50} values for each cell line \pm SD are displayed in the legend. (F) Graphs showing % change in apoptotic cell subpopulations for FT240, HEYA8, OVCAR8, and OVCAR4 cell lines treated with either 0, 1, or 10 μM CF for 48 hours. (G) Graphs showing % change in cell cycle subpopulations for FT240, HEYA8, OVCAR8, and OVCAR4 cell lines treated with either 0, 1, or 10 μM CF for 48 hours. All statistical comparisons are between CF versus vehicle treatment within a subpopulation for a given cell line. All data [(A) to (G)] are representative of $N = 3$ biological replicates. Statistical comparisons of two groups were performed using Student's *t* test, and comparisons of three or more groups were performed using one-way ANOVA with Tukey multiple testing correction unless otherwise stated.

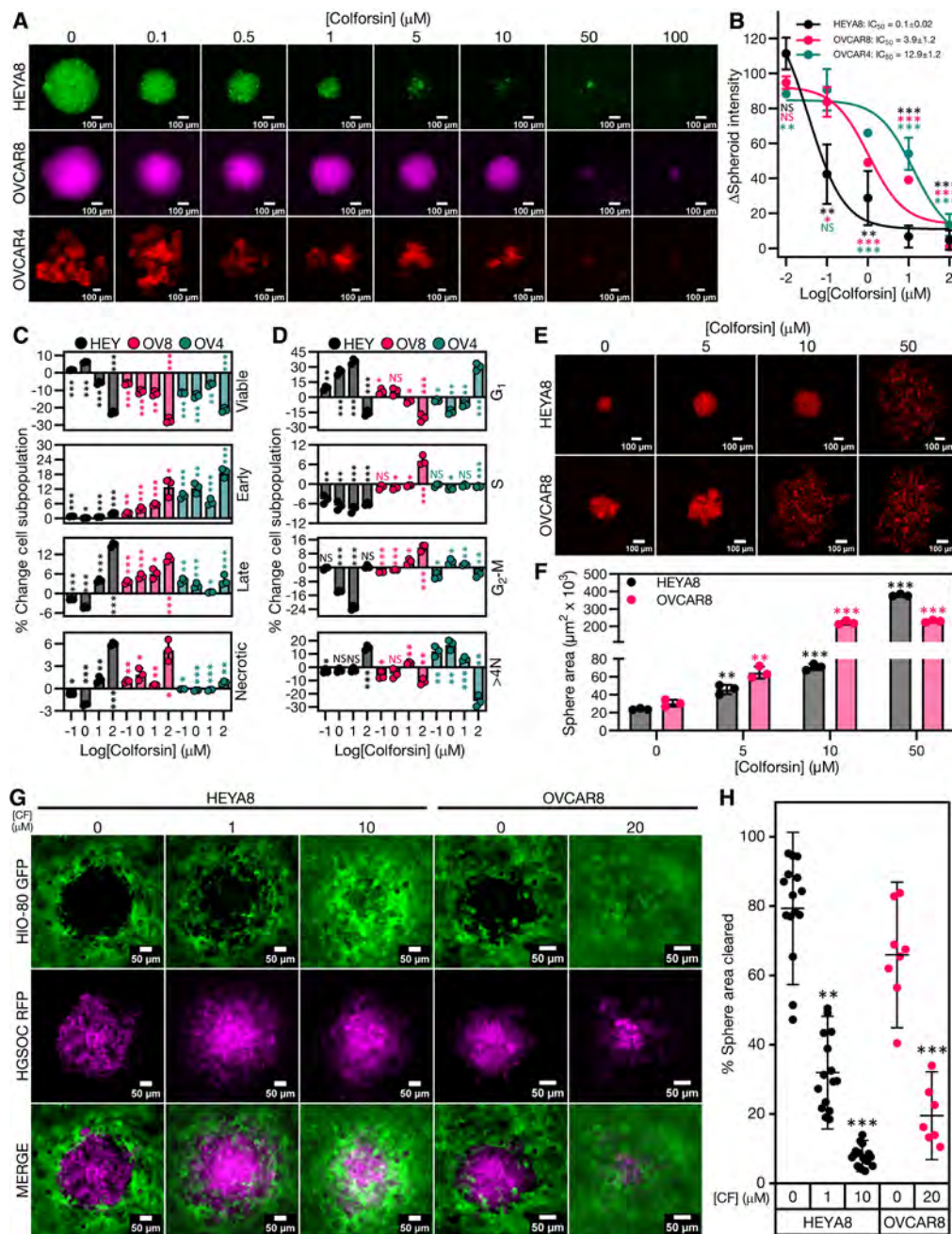


Fig. 2. CF inhibits growth of ovarian cancer spheroids. (A) Representative fluorescence micrographs of ovarian cancer spheroids after 7 days of culture under ULA conditions in medium containing either vehicle or increasing doses of CF. Spheroids are shown in pseudocolor to highlight different cell lines. Scale bars for images are 100 μm . A minimum of three spheroid formation wells (technical replicates) were analyzed in each of three biological replicates. (B) Graph showing dose-response curves for ovarian cancer spheroids cultured in either vehicle or increasing doses of CF. Mean IC_{50} values \pm SD are displayed in the upper right corner for each cell line. All statistical comparisons are between a given CF dose versus vehicle control within each cell line. (C) Graphs showing % change in apoptotic cell subpopulations for FTSEC and ovarian cancer spheroids in response to treatment with either vehicle or increasing doses of CF. All statistical comparisons are between a given CF dose versus vehicle control within each cell line. (D) Graphs showing % change in cell cycle subpopulations for FTSEC and ovarian cancer spheroids in response to treatment with either vehicle or increasing doses of CF. All statistical comparisons are between a given CF dose versus vehicle control within each cell line. (E) Representative micrographs of vehicle- and CF-treated HGSOC spheroid formation at 18 hours under ULA culture conditions. Scale bars for images are 100 μm . A minimum of three spheroid formation wells (technical replicates) were analyzed in each of three biological replicates. (F) Graph with quantification of sphere area for vehicle- and CF-treated spheres shown in (E). (G) Representative fluorescence micrographs of vehicle- or CF-treated HEYA8 or OVCAR8 RFP ovarian cancer spheroid clearance of HIO-80 GFP OSE cell monolayers. Scale bars for images are 50 μm . HGSOC spheroids are shown in pseudocolor. Five spheroid adhesion wells (technical replicates) were analyzed in each of three biological replicates. (H) Graph showing quantification of % sphere area cleared for the images shown in (G). All data [(A) to (H)] are representative of $N = 3$ biological replicates. Statistical comparisons of two groups were performed using Student's t test, and comparisons of three or more groups were performed using one-way ANOVA with Tukey multiple testing correction unless otherwise stated.

is a key factor necessary for the cells to survive and metastasize as spheroids (53). We observed that CF inhibited the ability of HGSOC cells to form tight spheroids (Fig. 2E). Treatment of HGSOC cells in two-dimensional (2D) culture with 5 μM CF before seeding under ULA conditions produced a two- to threefold increase in sphere size versus vehicle, indicating inhibition of tight sphere formation (Fig. 2F). Pathway analysis data also indicated inhibition of integrin signaling, adherens junction signaling, and adhesion molecules (such as NECTIN1 and TNS1) in response to increasing doses of CF (fig. S9A). After the observation of CF-induced spheroid disruption, we wanted to determine whether this affected the functional capacity of the spheroids to adhere to and invade an epithelial monolayer. We used an established epithelial clearance assay using vehicle- or CF-treated HGSOC red fluorescent protein (RFP) spheroids seeded on top of a green fluorescent protein-positive (GFP⁺) HIO-80 OSE cell monolayer (54). We observed that CF inhibited the ability of the HGSOC-RFP spheroids to clear and invade the OSE monolayer in a dose-dependent manner (Fig. 2, G and H). Together, these data show that HGSOC spheroids, the metastatic vehicle for ovarian cancer, remain sensitive to CF and that CF inhibits the ability of HGSOC spheroids to invade an epithelial cell monolayer.

Cis and CF synergize to induce ovarian cancer cell death

On the basis of previous reports that forskolin could have additive or synergistic effects when combined with traditional chemotherapies (30), we next investigated the combinatorial treatment of CF with Cis in the OVCAR8 and OVCAR4 cell lines, which were less sensitive to CF as a monotherapy. CF displayed synergy with Cis treatment as measured by combinatorial dose-response matrix cell viability assays in OVCAR8 and OVCAR4 cells (Fig. 3, A to C). Synergy scores calculated with SynergyFinderPlus software showed synergistic responses for most drug combinations in both cell lines (Fig. 3B) (55). We also calculated synergy for the dose-response matrices using the coefficient of drug interaction (CDI) (56) and found that most dose combinations resulted in a CDI of <1, confirming synergy between CF and Cis in OVCAR8 and OVCAR4 cells (Fig. 3C). We also examined their synergy in our panel of PDX cell lines, wherein, again, synergistic responses were observed for most CF + Cis combination doses as calculated with SynergyFinder or the CDI (Fig. 3, D and E, and fig. S4A). Notably, synergy scores were higher in the Cis-resistant than in the Cis-sensitive cell lines (Fig. 3E). In addition, synergy between CF and Cis was not observed in normal IMR90 fibroblasts (fig. S4, B and C).

Next, we investigated the effects of CF-Cis combination treatment on clonogenic survival and colony formation for OVCAR8 and OVCAR4 cells (Fig. 3, F to H). We again observed a synergistic response to combinations of CF and Cis (Fig. 3H). Analysis of apoptosis for the combination treatment of OVCAR8 and OVCAR4 cells demonstrated increases in apoptotic subpopulations for both cell lines compared with either single agent, particularly at lower doses (Fig. 3I). In the OVCAR8 cells, early apoptotic cells increased approximately two- to threefold for the combination versus CF or Cis alone at a dose of 1 μM . For OVCAR4 cells, there was a notable increase in necrotic cells at 1 μM combination (10% subpopulation change) versus either single agent (0.3% and 0.5% for CF and Cis, respectively). With respect to the cell cycle, increases in G₂-M accumulation were increased in the combination- versus single agent-treated OVCAR8 cells (Fig. 3J). The OVCAR4 cells also showed increased aneuploid accumulation when treated with the combination versus either single

agent (Fig. 3J). Combined, these data indicate that CF can synergize with Cis to induce cell death and cell cycle arrest in HGSOC cell lines.

CF inhibits ovarian cancer growth in vivo

After observing the capacity of CF to induce HGSOC cell death in culture, we next investigated whether CF could inhibit tumor growth in vivo. For these experiments, we used a subcutaneous tumor formation model using the more sensitive HEYA8 cells to determine efficacy of CF in a single, localized tumor and determine whether CF and Cis displayed any synergistic activity in vivo. We also used an orthotopic intraperitoneal tumor formation model with CF-resistant OVCAR4 cells to determine efficacy of systemic CF administration in the context of metastatic dissemination. For the subcutaneous model, HEYA8 tumors were allowed to grow to 100 mm³, randomized, and then treated with either phosphate-buffered saline (PBS) vehicle, CF, Cis, or the CF-Cis combination via intratumor injection (Fig. 4A). We found that CF treatment was able to inhibit tumor growth (Fig. 4, B and C). Initially, CF treatment was able to cause partial regression of tumor size for the first 2 weeks before tumors started to grow beyond baseline (Fig. 4C). Cis monotherapy performed comparably to CF in terms of tumor kinetics, particularly at later time points (Fig. 4C). The combination treatment of CF and Cis showed the best response with a more pronounced inhibition of tumor growth (Fig. 4C). The combination treatment also had the best profile with respect to tumor progression with regression in tumor size that was sustained for approximately 3 weeks (Fig. 4C). We analyzed the subcutaneous tumor kinetics data with combPDX software to determine whether CF and Cis were synergistic in vivo (57). Combination indices (CIs) for the combined CF + Cis treatment arm were greater than 1 (indicating synergy) from days 14 to 48 when generated using either the Bliss independence or highest single agent (HSA) method (Fig. 4D). In terms of histology, all tumors had morphology features consistent with HGSOC and stained positive for the mullerian marker PAX8 (Fig. 4E). However, it was observed that vehicle-treated tumors had a higher percentage of proliferative (Ki-67-positive) cells than CF-treated tumors (Fig. 4, E and F). In addition, the combination-treated tumors had a lower percentage of Ki-67-positive cells than tumors treated with either the CF or Cis alone (Fig. 4, E and F). With respect to final tumor burden, we found that the CF + Cis combination treatment followed by CF monotherapy and then Cis monotherapy produced the largest to smallest decrease in final tumor mass, respectively (Fig. 4G and fig. S5A).

We also observed synergy between CF and Cis in the OVCAR4 intraperitoneal model of metastatic dissemination. After intraperitoneal injection and randomization, we observed that CF treatment produced a robust growth inhibition response, whereas tumor growth inhibition was less pronounced in Cis-treated mice (Fig. 4, H to J, and fig. S5B). Combination treatment produced the greatest response outperforming either monotherapy (Fig. 4, I and J, and fig. S5B). Combination treatment of tumors produced sustained tumor growth regression that persisted even after treatment was stopped (Fig. 4, I and J, and fig. S5B). Analysis of tumor kinetic data with combPDX showed CIs greater than 1 from day 21 onward using both Bliss and HSA methods (Fig. 4K). In addition, survival analysis demonstrated that CF monotherapy significantly extended survival compared with vehicle or Cis (Fig. 4L). Combination treatment resulted in the largest survival increase outperforming either monotherapy (Fig. 4L). Notably, we did not observe any overt drug toxicity in CF- or combination-treated mice, and there were no statistically significant differences in

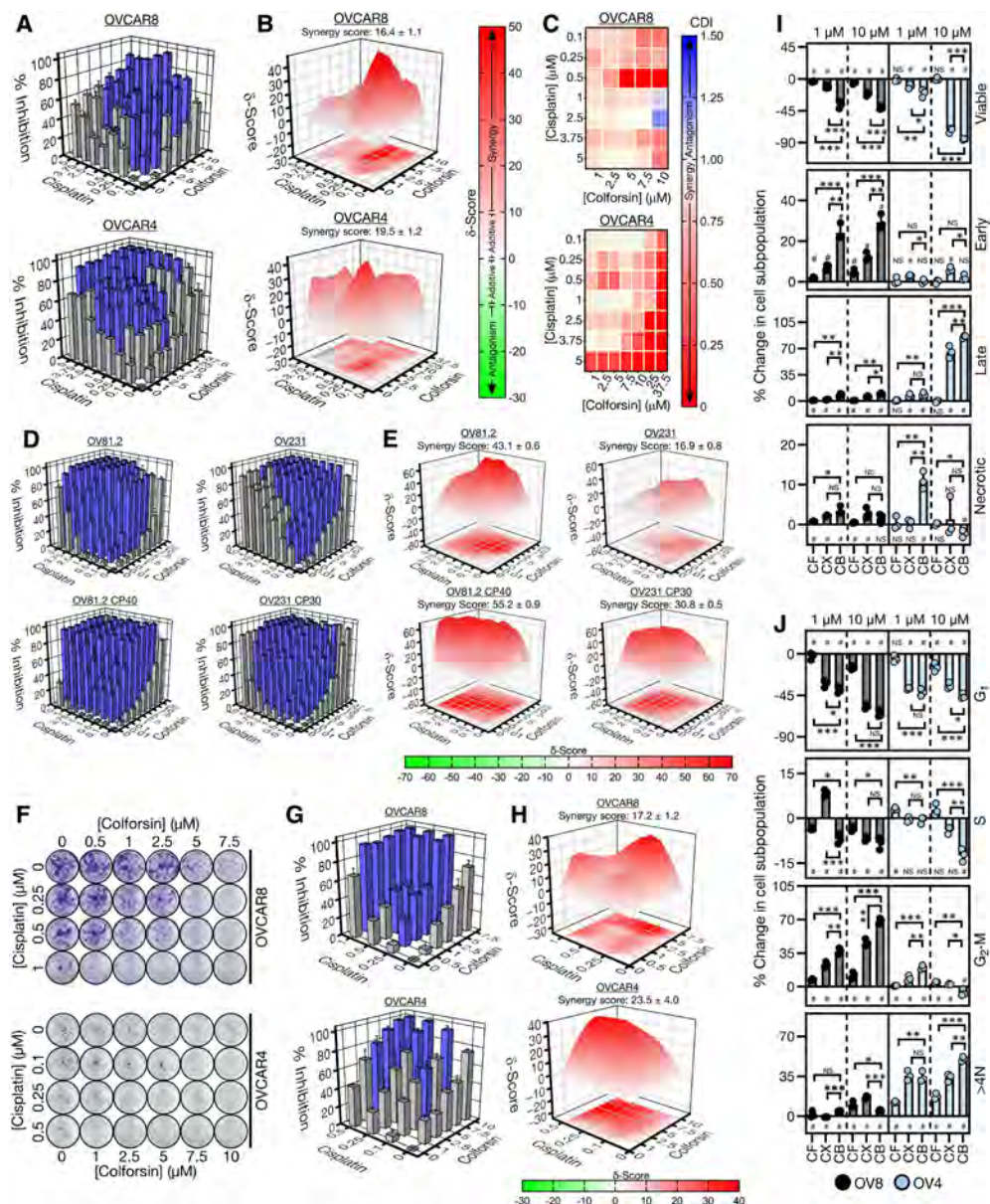


Fig. 3. CF synergizes with Cis to cause HGSOc cell death in culture. (A) 3D bar graphs showing % cell viability inhibition for CF-Cis combination dose-response matrices in OVCAR8 cells (top) and OVCAR4 cells (bottom). Blue bars indicate dose combinations that were significantly different from the corresponding single-agent dose. (B) 3D surface colormap for Bliss/Loewe consensus δ synergy scores of CF-Cis combination dose-response matrices in OVCAR8 cells (top) and OVCAR4 cells (bottom). Overall synergy scores \pm SD are displayed above each graph. Synergy scores less than -10 indicate antagonism; synergy scores from -10 to 0 and 0 to 10 indicate additive interaction in either the negative or positive direction, respectively; and synergy scores greater than 10 indicate synergy for a given dose combination. (C) Heatmaps of the CDI for OVCAR8 cells (top) and OVCAR4 cells (bottom). CDI values less than 1 indicate synergy, CDI values equal to 1 indicate additive interaction, and CDI values greater than 1 indicate antagonism for a given dose combination. (D) 3D bar graphs showing % cell viability inhibition for CF-Cis combination dose-response matrices in OV81.2, OV81.2 CP40, OV231, and OV231 CP30 cells. Blue bars indicate dose combinations that were significantly different from the corresponding single-agent dose. (E) 3D surface colormap for Bliss/Loewe consensus δ synergy scores of CF-Cis combination dose-response matrices in OV81.2, OV81.2 CP40, OV231, and OV231 CP30 cells. Overall synergy scores \pm SD are displayed above each graph. (F) Representative images of wells from OVCAR8 (top) and OVCAR4 (bottom) clonogenic CF-Cis dose-response matrices. (G) 3D bar graphs showing % colony area inhibition for CF-Cis combination dose-response matrices in OVCAR8 cells (top) and OVCAR4 cells (bottom). Blue bars indicate dose combinations that were significantly different from the corresponding single-agent dose. (H) 3D surface colormap for Bliss/Loewe consensus δ synergy scores of clonogenic CF-Cis combination dose-response matrices in OVCAR8 cells (left) and OVCAR4 cells (right). Overall synergy scores \pm SD are displayed above each graph. (I) Graphs showing % change in apoptotic subpopulations for OVCAR8 and OVCAR4 cells when treated with either CF, Cis, or a combination of CF and Cis at a 1:1 ratio. # indicates statistical significance ($P \leq 0.05$) for comparison of a particular treatment subpopulation with the vehicle control. (J) Graphs showing % change in cell cycle subpopulations for OVCAR8 and OVCAR4 cells when treated with either CF, Cis, or a combination of CF and Cis at a 1:1 ratio. # indicates statistical significance ($P \leq 0.05$) for comparison of a particular treatment subpopulation with the vehicle control. CF, colforsin daropate; CX, Cis; CB, combination. All data [(A) to (J)] are representative of $N = 3$ biological replicates. Statistical comparisons of two groups were performed using Student's t test, and comparisons of three or more groups were performed using one-way ANOVA with Tukey multiple testing correction unless otherwise stated.

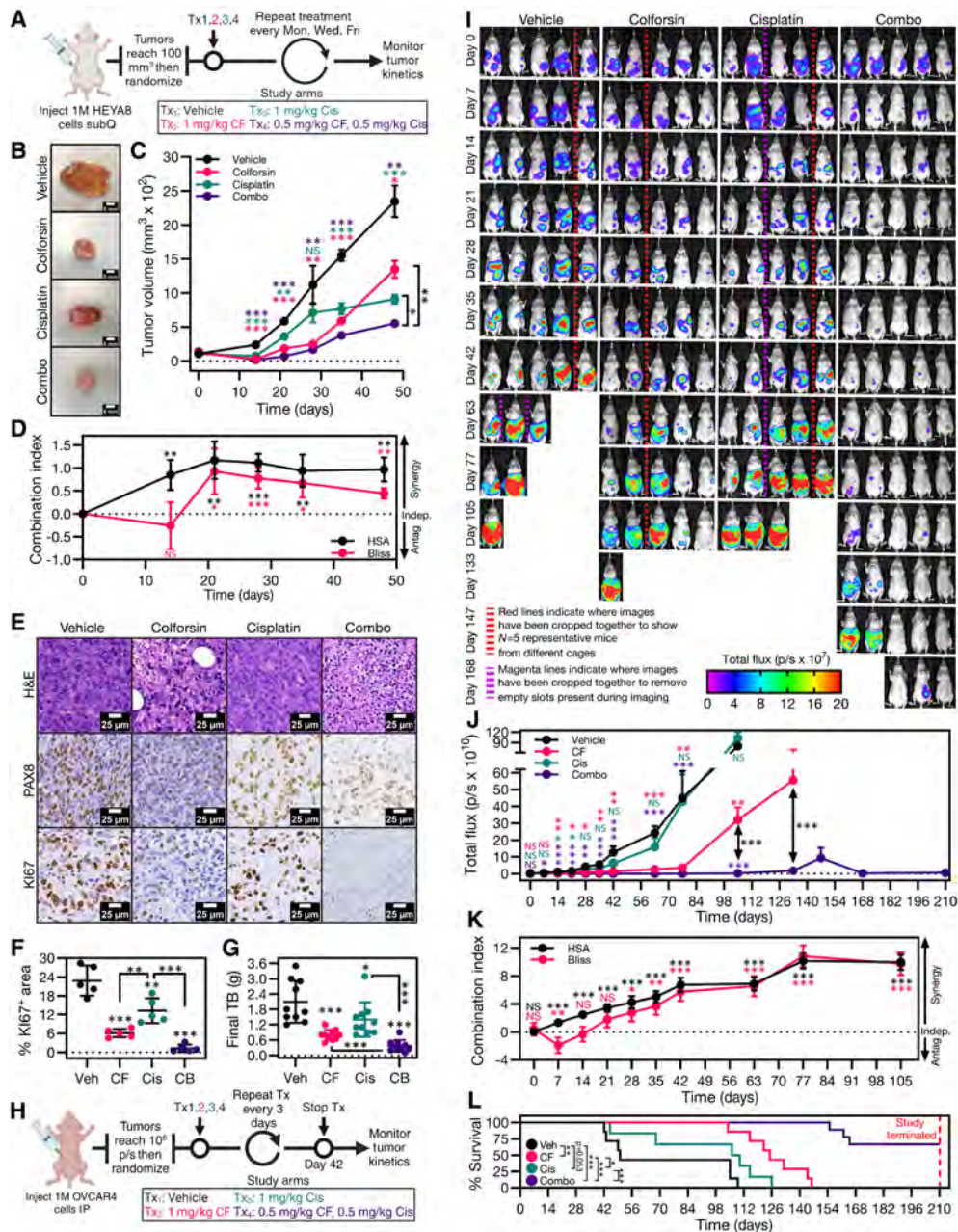


Fig. 4. CF inhibits HGSOc tumor growth in vivo. (A) Diagram depicting dosing schedule for HEYA8 subcutaneous tumor formation experiment. (B) Representative images of subcutaneous HEYA8 tumors harvested from mice treated with either vehicle, CF, Cis, or the 1:1 CF-Cis combination. (C) Graph of tumor kinetics for mice treated with either vehicle, CF, Cis, or the 1:1 CF-Cis combination. Error bars represent \pm SEM. (D) Graph of Bliss and HSA in vivo synergy CIs for CF-Cis-treated HEYA8 tumors. A CI greater than 0 represents synergy between the two treatment groups, a CI equal to 0 represents independent effects for the two treatment groups, and a CI less than 0 represents antagonism between the two treatment groups. (E) Representative micrographs of hematoxylin and eosin (H&E), PAX8, and Ki-67 staining of vehicle-, CF-, Cis-, and 1:1 CF-Cis combination-treated tumors. Scale bars for images are 25 μ m. (F) Graph showing % positive area for Ki-67 in vehicle-, CF-, Cis-, or 1:1 CF-Cis combination-treated tumors. (G) Graph showing final tumor burden for vehicle-, CF-, Cis-, or 1:1 CF-Cis combination-treated tumors. (H) Diagram depicting dosing schedule for OVCAR4-Luc intraperitoneal (IP) tumor formation experiment. (I) Representative bioluminescence images of intraperitoneal tumor kinetics at days 0 to 168 for mice treated with either vehicle, CF, Cis, or the 1:1 CF-Cis combination. Red lines indicate where images have been cropped together to show N = 5 representative mice from different cages. Magenta lines indicate where images have been cropped together to remove empty slots present during imaging. (J) Graph of intra-peritoneal tumor kinetics for mice treated with either vehicle, CF, Cis, or the 1:1 CF-Cis combination. Error bars represent \pm SEM. (K) Graph of Bliss and HSA in vivo synergy CIs for CF-Cis-treated OVCAR4-Luc tumors. (L) Kaplan-Meier survival curves for OVCAR4-Luc mice treated with either vehicle, CF, Cis, or the 1:1 CF-Cis combination. Statistical comparisons between treatment groups are shown next to the legend and were performed using the log-rank test. Dashed red line indicates the time point where the study was terminated and all surviving mice were euthanized. All data [(A) to (L)] are representative of at least N = 3 biological replicates. For all in vivo experiments, N \geq 5 mice for each treatment group. Statistical comparisons of two groups were performed using Student's *t* test, and comparisons of three or more groups were performed using one-way ANOVA with Tukey multiple testing correction unless otherwise stated.

body weight between the drug-treated versus vehicle-treated mice when treatment was stopped (fig. S5C). Together, these data show that CF can inhibit HGSOc tumor growth and that combination treatment with CF and Cis can generate more durable tumor growth inhibition than either monotherapy.

EIF2 and MYC signaling are inhibited in CF-treated ovarian cancer cells

After the observations of therapeutic efficacy for CF in cell culture and in vivo, we next wanted to elucidate which signaling pathways were altered in CF-treated HGSOc cells that could drive the observed antitumor phenotypes. To identify key signaling pathways in CF versus vehicle-treated HGSOc cells, we treated HEYA8 cells with either vehicle or increasing doses of CF and then performed bulk RNA sequencing to profile transcriptional changes in HEYA8 cells at the various CF doses (Fig. 5A). We then applied a criterion filter to the sequencing data so that only genes whose expression was significantly increased or decreased by CF treatment versus the vehicle by a fold change of 1.5 (≤ -1.5 or ≥ 1.5 , with a multiple testing corrected $P < 0.01$) were included in further analysis. The total number of differentially expressed genes (DEGs) increased as a function of the CF dose, with 1 μ M CF having approximately 600 DEGs and 10 μ M having approximately 2300 DEGs (Fig. 5B), indicating a dynamic response in the transcriptional profile of the cells to CF. Varying degrees of DEG overlap were observed between the different CF doses, with a core network of 460 DEGs common to all three doses (Fig. 5C).

Next, we examined the DEGs of each CF dose using ingenuity pathway analysis (IPA) to identify which signaling pathways were differentially altered in CF- versus vehicle-treated HEYA8 cells. Comparison analysis of canonical signaling pathways in the different CF-treated samples identified several hits with relevance to our observed phenotypes (Fig. 5D). The top two canonical pathways that had significant overlap with the DEGs of the CF-treated samples were “EIF2 signaling” and “cell cycle control of chromosomal replication,” both of which were predicted to be down-regulated in response to CF treatment (Fig. 5D). EIF2 signaling is a key pathway involved in ribosome assembly and protein translation that is frequently dysregulated in cancer (58). The “cell cycle control of chromosomal replication pathway” contains key signaling molecules that facilitate DNA replication and G₁-S transition. Notably, inhibition of both pathways can lead to the cell death and cell cycle arrest phenotypes we observed when HGSOc cells were treated with CF. We also observed up-regulation of cell cycle checkpoint pathways such as G₁-S checkpoint regulation (Fig. 5D). Curiously, we did not see strong activation of cAMP or PKA signaling pathways (contrary to expectations, given the canonical function of CF as an AC activator), although there was significant overlap between these pathways and the DEGs of CF-treated HEYA8 cells (Fig. 5D and fig. S6A). More detailed functional analysis confirmed that CF-treated HEYA8 cells did not produce increased intracellular cAMP as measured by cAMP Glo assay (fig. S6B). Levels of phosphorylated CREB also did not increase in CF-treated HGSOc cells (fig. S6, C and D). These data suggested that CF was increasing cell cycle arrest and cell death in the HEYA8 cells through a noncanonical mechanism. Alternatively, there may be strong negative feedback by phosphodiesterase (PDE)-mediated hydrolysis, given that there was a 3- to 10-fold up-regulation of multiple PDEs, including cAMP-selective PDE4 and PDE7, in CF-treated cells (fig. S6A).

Further analysis of the functional signaling pathways that were altered in the CF-treated cells again produced several hits relevant to our observed phenotype. This included predicted activation, and significant overlap, of several cell death pathways such as “cell death of cancer cells” and “necrosis of tumor” (Fig. 5D and fig. S7, A to C). It also included predicted inhibition of cell proliferation and migration/invasion pathways (Fig. 5D and fig. S7, A to C). After the analysis of CF-induced pathway alterations at a global level, we focused on EIF2 signaling in more detail to further elucidate which components of the pathway were down-regulated. We found that several eIF family members were down-regulated including eIF1, eIF2A, and several subunits of eIF3 (Fig. 5E). In addition, many ribosomal proteins were down-regulated in response to CF treatment including several members of both the small and large ribosomal subunit complexes (Fig. 5E). On the basis of these data, we used IPA to identify predicted upstream regulators that could modulate expression of both eIFs and ribosomal proteins as well as the CF-induced pathway changes we observed. The top predicted upstream regulator for these criteria was the well-known oncogenic transcription factor c-MYC. Sixty-seven of the DEGs present in the CF-treated HEYA8 cells (~34 to 37%) were common to both the EIF2 signaling pathway and MYC upstream regulator pathway (Fig. 5F). MYC RNA levels were decreased in response to CF treatment (Fig. 5E), and MYC signaling was predicted to be inhibited in response to CF treatment (Fig. 5G). Together, the results of our pathway analysis indicated that CF-induced cell cycle arrest and cell death were likely mediated through inhibition of MYC and EIF2 signaling.

CF inhibits MYC to induce ovarian cancer cell death

The results of our pathway analysis indicated that CF may be inhibiting MYC signaling to drive HGSOc cell cycle arrest/cell death. Therefore, we next investigated the functional relationship between CF and MYC. MYC is an established driver of HGSOc and is amplified at the copy number and protein levels in up to 50% of patients with HGSOc (59). We observed that several MYC targets were decreased at the mRNA level in HEYA8 cells treated with CF (Fig. 5H). We next examined protein levels of downstream MYC targets involved in translation and cell cycle progression whose down-regulation could contribute to the cell cycle arrest/cell death phenotypes we observed in CF-treated HGSOc cells. We observed decreased levels of cell cycle regulator proteins, such as BUB1 and Cdc20, and of several MYC-regulated translation factors, such as E2F1, eIF2 α , eIF4E, RPS12, and RPS16, as well as of phosphorylated eukaryotic translation initiation factor 4E binding protein-1 (p-4EBP1), a master regulator of protein synthesis (Fig. 6A). Phosphorylation of 4EBP1 prevents it from binding to eukaryotic translation initiation factor 4E (eIF4E) and inhibits formation of the translation initiation complex (60). Notably, increased levels of nonphosphorylated 4EBP1, observed in the CF-treated HEYA8 cells (Fig. 6A), have been linked to promoting cell cycle arrest and apoptosis in other cancer contexts (61–64). In OVCAR8 and OVCAR4 cells, MYC and its downstream targets were less responsive to CF treatment (Fig. 6B).

MYC nuclear localization was also decreased in response to CF treatment as measured by immunofluorescence (Fig. 6, C and D). We then validated that the decreases in MYC protein levels caused by CF corresponded to decreased MYC transcriptional activity using an established E-box luciferase reporter. We found that E-box reporter activity decreased in response to increasing CF dose in HGSOc cells (Fig. 6E). MYC protein levels correlated with CF

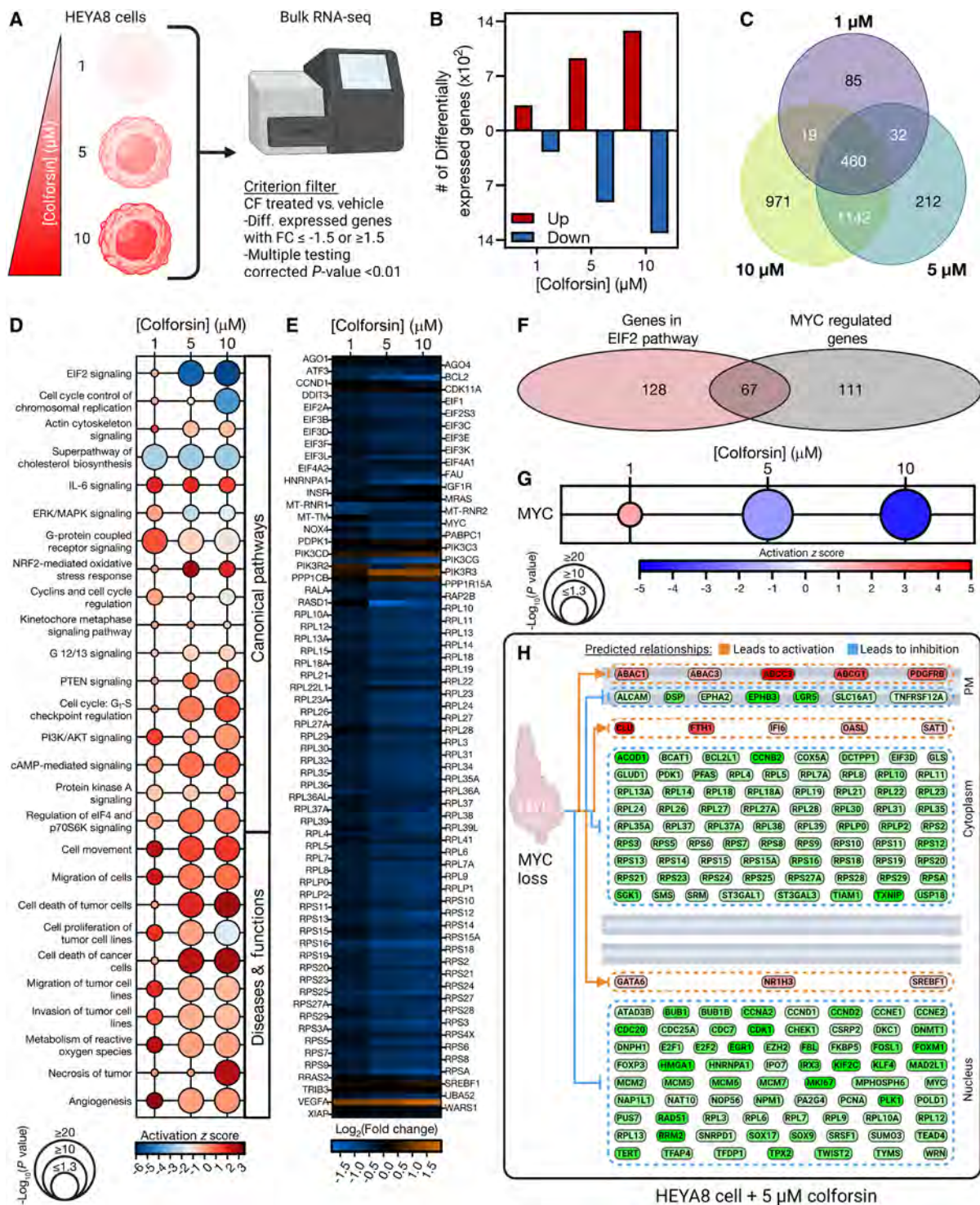


Fig. 5. EIF2 and MYC signaling are down-regulated in CF-treated HGSOC cells. (A) Diagram of experimental setup for bulk RNA sequencing of HEYA8 cells treated with either vehicle, 1, 5, or 10 μM CF. (B) Graph showing number of up- and down-regulated DEGs for each CF dose displayed below. (C) Venn diagram of DEG overlap for each CF dose. (D) Matrix bubble graph showing top differentially regulated canonical and functional pathways for CF-treated HEYA8 cells versus vehicle-treated HEYA8 cells. Significance values and activation z-scores for each pathway were computed using IPA software. (E) Heatmap showing gene expression changes in CF- versus vehicle-treated HEYA8 cells for genes in the EIF2 pathway. (F) Venn diagram showing overlap of DEGs common to both the EIF2 signaling pathway and MYC upstream regulator pathway that are present in HEYA8 cells treated with 10 μM CF. (G) Matrix bubble graph showing statistical significance and predicted activation z-score for the MYC upstream regulator pathway in CF-treated HEYA8 cells. Significance values and activation z-scores for each pathway were computed using IPA software. (H) Diagram showing RNA-sequencing expression levels of MYC targets in HEYA8 cells treated with 5 μM CF. All data [(A) to (H)] are representative of $N = 3$ biological replicates. Statistical comparisons of two groups were performed using Student's t test, and comparisons of three or more groups were performed using one-way ANOVA with Tukey multiple testing correction unless otherwise stated.

Downloaded from https://www.science.org at University of Pennsylvania on November 20, 2024

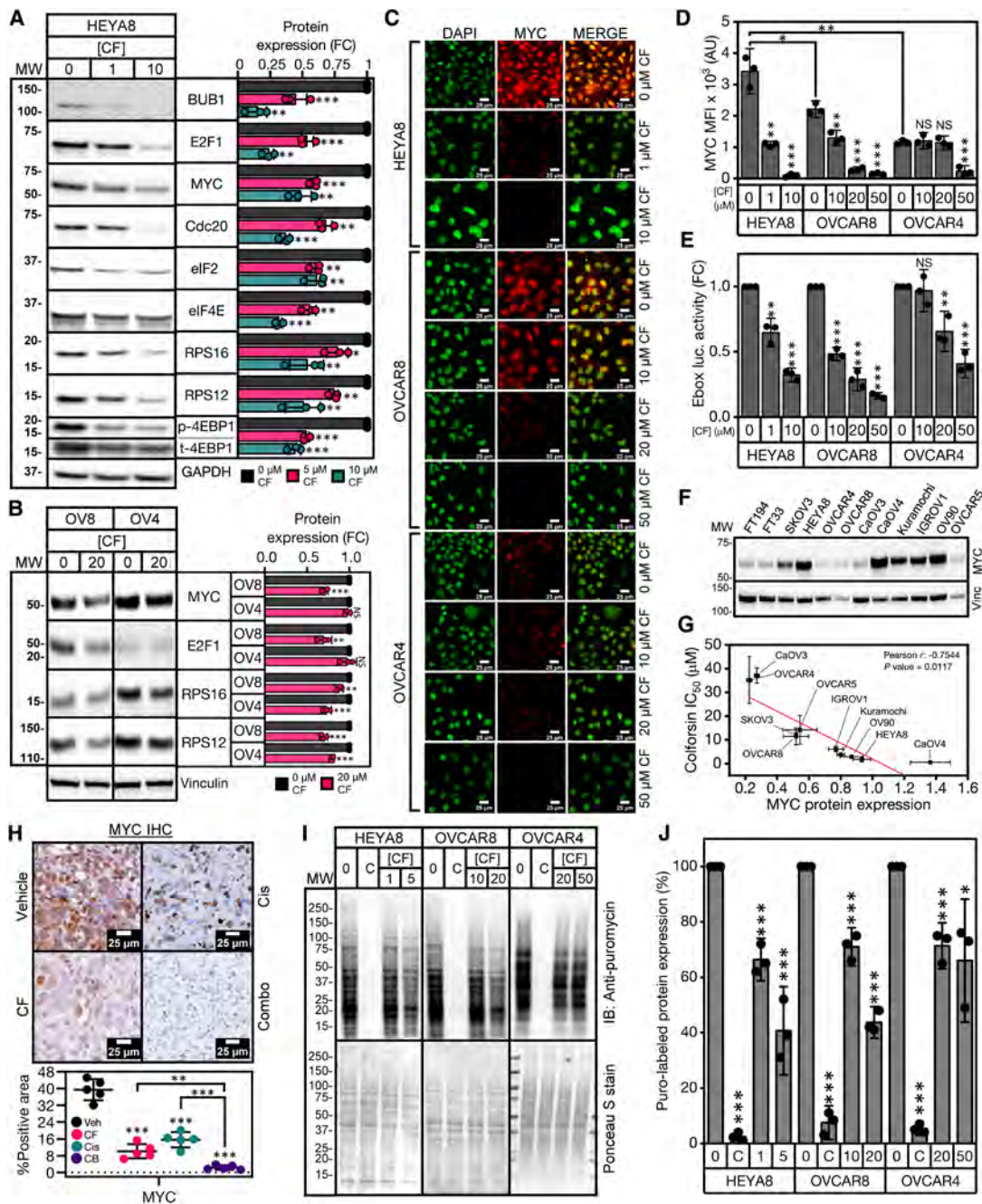


Fig. 6. CF decreases MYC levels to facilitate HGSOC cell death. (A) Representative Western blots of HEYA8 cells showing dose-dependent decreased levels of MYC protein and downstream MYC-regulated targets in response to CF treatment with quantification (right). An immunoblot of phosphorylated 4EBP1 (p-4EBP1) is shown above an immunoblot of total 4EBP1 (t-4EBP1) in a split panel. For quantification of p-4EBP1, p-4EBP1 levels were normalized to total 4EBP1 levels in each sample before normalization of CF-treated samples to vehicle. (B) Representative Western blots of OVCAR8 and OVCAR4 cells showing levels of MYC protein and downstream MYC-regulated targets in response to CF treatment with quantification (right). (C) Representative immunofluorescence images of MYC staining for HGSOC cells treated with CF for 48 hours. Scale bars for images are 25 μm. Five fields of at least 20 cells were analyzed in each of three biological replicates. (D) Quantification of nuclear MYC fluorescence for HGSOC cells treated with CF for 48 hours. (E) Quantification of E-box luciferase activity for HGSOC cells treated with CF for 48 hours. (F) Western blot of MYC expression across a panel of FTSEC and HGSOC cell lines. (G) Correlation plot of CF IC₅₀ values versus MYC protein expression for the panel of HGSOC cell lines shown in (F). The Pearson *r* correlation coefficient along with the corresponding *P* value are shown in the upper right corner of the graph. (H) Representative micrographs of MYC staining of HEYA8 vehicle, CF, Cis, and 1:1 CF-Cis combination-treated tumors with quantification below. Scale bars for images are 25 μm. (I) Detection of nascent polypeptides via puromycin labeling of HGSOC cells treated with either vehicle, CF, or cycloheximide (50 μg/ml) ("C"). Western blot of lysates using anti-puromycin antibody (top) and Ponceau S staining of lysates measuring total protein levels (bottom). (J) Graph showing quantification of % puromycin labeling of drug-treated lysates relative to vehicle. All data [(A) to (J)] are representative of *N* = 3 biological replicates. Statistical comparisons of two groups were performed using Student's *t* test, and comparisons of three or more groups were performed using one-way ANOVA with Tukey multiple testing correction unless otherwise stated.

Downloaded from https://www.science.org at University of Pennsylvania on November 20, 2024

sensitivity in a panel of HGSOC cell lines (Fig. 6, F and G). Notably, two of the most CF-sensitive cell lines, CaOV4 and Kuramochi, had MYC amplification (in copy number, protein expression, and signaling activity; table S1). In addition, MYC levels were reduced in the CF- and Cis (single agent)-treated HEYA8 tumors by approximately 50% and in combination-treated tumors by >90% compared with vehicle-treated tumors (Fig. 6H). These data indicated that CF and Cis acted synergistically to decrease MYC in the HEYA8 tumors. To validate that CF was inhibiting translation, we performed a puromycin labeling assay to identify nascent polypeptides in vehicle- and CF-treated HGSOC cells. We observed that CF treatment reduced global protein synthesis in HGSOC cells in a dose-dependent manner (Fig. 6, I and J). In addition, the levels of translation inhibition achieved with CF treatment corresponded to the relative CF sensitivity of the HGSOC cell lines tested (Fig. 6, G, I, and J).

To investigate the functional relationship between CF and MYC, we profiled the response of isogenic FTSECs that were transformed into HGSOC with overexpression of either MYC or a different oncogene. We hypothesized that because the antitumorigenic effects of CF are mediated at least in part by decreasing MYC expression, FTSECs transformed with MYC should be more sensitive to CF than those transformed with a different oncogene. Specifically, the FTSEC lines used included FT33 +EV (immortalized with SV40 large T antigen, not transformed, EV indicates empty vector), FT33 +MYC (immortalized with SV40 large T antigen, transformed with degradable MYC overexpression), FT33 +Ras (immortalized with SV40 large T antigen, transformed with Ras overexpression), FT194 +EV (immortalized with SV40 large T antigen, not transformed), FT194 +MYC (immortalized with SV40 large T antigen, transformed with degradable MYC overexpression), and FT194 +YAP (immortalized with SV40 large T antigen, transformed with YAP overexpression). We observed that the MYC-transformed FT cell lines were more sensitive to CF treatment than the Ras- or YAP-transformed cell lines (Fig. 7A). As expected, the nontransformed FT cell lines were the least responsive to CF and had the highest IC₅₀ values (Fig. 7A). The CF-treated, MYC-transformed FTSEC cell lines also exhibited increased levels of apoptosis compared with the Ras- or YAP-transformed cell lines (Fig. 7, B and C). With respect to MYC signaling, we found that the MYC-transformed FT33 cells had larger decreases in MYC and MYC target levels than either the FT33 +Ras or FT33 +EV cells when treated with CF (Fig. 7, D and E). We also investigated the effects of transient MYC depletion on HGSOC sensitivity to CF treatment. HEYA8 and CaOV4 cells were transfected with MYC small interfering RNA (siRNA) and then cultured in either vehicle- or CF-containing medium. We observed a baseline reduction in proliferation of vehicle-treated HGSOC cell lines when MYC was knocked down (fig. S8, A to C). Notably, transient MYC knockdown diminished the ability of CF to inhibit proliferation of the HGSOC cells, as indicated by the increase in IC₅₀ values in the siMYC-transfected cells (fig. S8D). Together, these data show that CF facilitates cell cycle arrest and cell death in HGSOC at least in part by decreasing MYC expression.

DISCUSSION

We wanted to determine whether CF, a water-soluble derivative of forskolin, could be repurposed for HGSOC treatment. CF induced cell death in established HGSOC cell lines, including clinically relevant PDX cell lines. Notably, immortalized, nontransformed FTSECs were far less

sensitive to CF than HGSOC cells, demonstrating that CF was selective for cancer versus “normal” cells of the reproductive tract. We observed differences in the type of cell cycle arrest/cell death for the different HGSOC cell lines that roughly corresponded to their sensitivity to CF overall. These data highlight the ability of CF to consistently produce a therapeutic response in a heterogeneous panel of HGSOC cell lines, suggesting that it will be effective in most patients with ovarian cancer.

It has been previously reported that ovarian cancer spheroids are protected from chemotherapy and demonstrate increased drug resistance compared with their 2D counterparts (65, 66). HGSOC spheroids were more sensitive to CF than the corresponding 2D culture. We observed here that the CF-treated spheroids showed a reduction in adhesion signaling and tended to be less compact than vehicle-treated spheroids. It is likely that CF decreases important intrinsic prosurvival signals in the spheroids that depend on cell-cell adhesion. This also allows the drug greater access to more tumor cells than would otherwise be possible. Future studies will need to investigate in detail the mechanisms by which CF disrupts ovarian cancer sphere adhesion.

Combination treatment of our HGSOC cell lines with CF + Cis produced synergism in therapeutic response for CF-resistant cells. In addition, CF-Cis synergy was more pronounced in the Cis-resistant versus Cis-sensitive PDX isogenic cell lines. These data suggest that CF may also have utility in resensitizing resistant disease to Cis. Forskolin treatment has been shown to produce increased Cis accumulation within ovarian cancer cells (30). Given the synergism observed between CF and Cis in our experiments, it is likely that this phenomenon occurs with CF as well. It will be important to confirm whether CF can increase Cis accumulation in HGSOC cells, elucidate the mechanism by which this occurs, and determine whether CF-enhanced Cis accumulation selectively occurs in cancer cells versus normal tissue.

We next wanted to determine CF efficacy for treating HGSOC in vivo. In the subcutaneous and intraperitoneal models, CF was effective as a monotherapy in reducing tumor kinetics and tumor burden, but CF-Cis combination therapy produced the largest and most durable response. Combination treatment was able to cause sustained intraperitoneal tumor regression that persisted even after treatment was stopped. Notably, analysis of tumor kinetics data with combPDX showed strong in vivo synergy for CF and Cis. These data provide proof of concept for the use of CF as an adjuvant therapy that can be incorporated into standard HGSOC chemotherapy regimens. Our results indicate that CF can inhibit the capacity of HGSOC spheroids to invade OSE monolayers; thus, we predict that CF will also be able to inhibit intraperitoneal metastasis as well.

Several changes in pathway expression were observed with CF treatment of HEYA8 cells that were consistent with increased tumor cell death and cell cycle arrest. The top pathway alteration was a significant down-regulation of EIF2 signaling, the primary pathway that controls translation and protein production. Further analysis revealed down-regulation of several ribosomal proteins and eIFs that are required to assemble ribosomal subunits. These changes in signaling are consistent with the observed CF-induced cell cycle arrest and cell death. Decreased ribosome production has been previously linked to increases in cell cycle arrest and cell death (67–71). In addition, inhibition of ribosome biogenesis as a cancer therapy is an active area of research (70).

Pathway analysis indicated that the top upstream signaling regulator was the transcription factor MYC, an established oncogene and

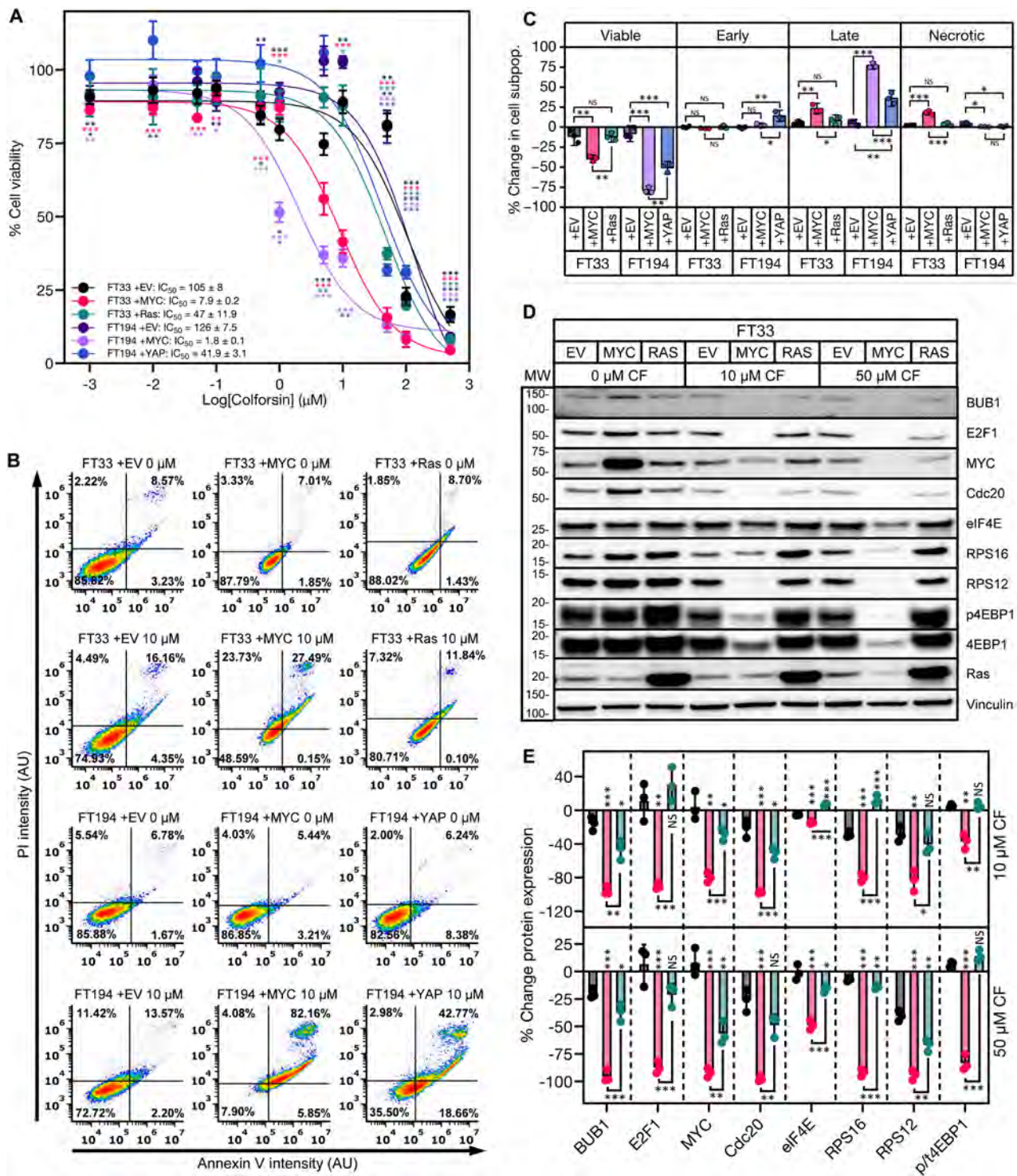


Fig. 7. Overexpression of MYC in FTSECs sensitizes them to CF treatment. (A) Dose-response curves of % cell viability for FT33 +TAG, FT33 +MYC, FT33 +Ras, FT194 +TAG, FT194 +MYC, and FT194 +YAP cells treated with increasing doses of CF. IC₅₀ values ± SD are shown in the legend. (B) Representative graphs showing annexin V-Pi staining for the FTSEC panel in response to treatment with 10 μM CF. (C) Graph showing % change in apoptotic cell subpopulations for the FTSEC panel in response to treatment with 10 μM CF. (D) Representative Western blots of the FTSEC panel showing dose-dependent decreased levels of MYC protein and downstream MYC-regulated targets in response to CF treatment. (E) Graph showing quantification of MYC and MYC-regulated targets in FT33 cells treated with CF. p/t4EBP1 corresponds to the ratio of phosphorylated to total 4EBP1. All data [(A) to (E)] are representative of N = 3 biological replicates. Statistical comparisons of two groups were performed using Student's t test, and comparisons of three or more groups were performed using one-way ANOVA with Tukey multiple testing correction unless otherwise stated.

master regulator of ribosome biogenesis. CF treatment was predicted to inhibit MYC activity, and MYC directly regulates many of the same genes found in the EIF2 pathway. CF treatment decreased MYC protein levels and transcriptional activity in HGSOc. Overexpression of MYC in isogenic FTSEC lines selectively sensitized them to CF versus other oncogenes. These results demonstrate that the anticancer effects of CF are mediated at least in part by inhibition of MYC. The CF-induced signaling changes we observed are particularly interesting because they indicate that the predominant mechanism of HGSOc cell death is noncanonical and independent of AC activation. Forskolin has been shown to bind to targets other than AC, and this may occur with CF as well (18).

This study establishes that CF has anticancer activity in HGSOc. Such activity is not, to our knowledge at the time of publication, demonstrated in any other cancer. Our data indicate that CF has robust cytotoxic effects that are selective for cancer cells versus nontransformed cells. The ability of CF to synergize with Cis opens the possibility for its use as an adjuvant to boost the efficacy of Cis in treating patients. CF inhibition of MYC protein expression is also highly relevant to HGSOc, given that the MYC gene is amplified in approximately 50% of HGSOcs. HGSOc cells in general are highly dependent on MYC for survival; however, therapeutic targeting of MYC has remained a challenge as the important functional domains of MYC are intrinsically disordered and not suitable for small-molecule binding (72, 73). Most drugs target MYC indirectly, and only a few can induce decreases in MYC protein levels (72). CF is therefore a novel and valuable addition to this subclass of drugs that can decrease MYC protein levels.

Several questions remain that will need to be addressed in future studies. The details of how CF decreases MYC levels in HGSOc and whether additional factors besides MYC are important CF targets will need to be elucidated. Further study will also be needed to determine the direct binding targets of CF in HGSOc cells. It will be important to determine whether CF derivatization can uncouple the anticancer effects from canonical effects to improve tolerability and minimize off-target effects. These questions will follow from our study's findings, which establish CF as a potential novel therapeutic for the treatment of MYC-driven HGSOc.

MATERIALS AND METHODS

Annexin V apoptosis assay

Cells were plated in six-well plates at a density of 200,000 cells per well. The next day, cells were treated with medium containing either CF, Cis, or the 1:1 CF-Cis combination for 48 hours. After drug treatment, the drug-containing medium was collected from each well to collect floating cells. Each well was then trypsinized to collect adherent cells, and the two cell fractions (floating + adherent) were pooled for each well. Detection of apoptosis was performed using the FITC Annexin V Apoptosis Detection Kit (BD, 556547) according to the manufacturer's protocol. Annexin V–fluorescein isothiocyanate (FITC) and PI emissions were measured for all samples using a BD Accuri flow cytometer with a minimum number of 10,000 cells measured per sample. Analysis and quantification of annexin V staining populations was performed using FCS Express software (DeNovo Software).

cAMP Glo assay

Cells were plated in six-well plates at 100,000 cells per well and treated the next day with either vehicle or CF for 72 hours. After 72 hours,

the cells were assayed to quantify intracellular cAMP levels according to the manufacturer's instructions.

Cell culture and reagents

Cells were cultured in 10-mm plates in a humidified atmosphere (5% CO₂) at 37°C. At 70 to 90% confluence, trypsin (0.25%)/EDTA solution was used to split the cells, which were used until passage 20. Cell culture medium (Corning) was supplemented with 10% fetal bovine serum (FBS) (Gibco) and 1% penicillin-streptomycin (PS) (Gibco) {HEYA8 cells [Dulbecco's minimum essential medium (DMEM)], FTSE cells (DMEM-F12), OVCAR8, OVCAR4 cells (RPMI)}. The following reagents were used in the study: Cis (Penn Hospital Pharmacy) and CF (Tocris, catalog no. 1099). All cell lines used in the study tested negative for mycoplasma and were validated using IDExx CellCheck.

Cell cycle assay

Cells were plated in 10-cm dishes at a density of 500,000 cells per well. The next day, cells were treated with medium containing either CF, Cis, or 1:1 CF-Cis combination for 48 hours. After drug treatment, the drug-containing medium was collected from each plate to collect floating cells. Each well was then trypsinized to collect adherent cells, and the two cell fractions (floating + adherent) were pooled for each well. Cells were washed in 1× PBS and then fixed in 70% EtOH overnight at –20°C. PI staining was performed using FxCycle PI/ribonuclease staining solution (Thermo Fisher Scientific, F10797) according to the manufacturer's protocol. PI emissions were measured for all samples using a BD Accuri flow cytometer with a minimum number of 10,000 cells measured per sample. Analysis and quantification of PI staining populations was performed using FCS Express software (DeNovo Software).

Cell viability assay

For the single-agent CF treatments, cells were plated in a 12-well plate at 50,000 cells per well and treated the next day with CF. After 48 hours, cells were then incubated with 3-(4,5-dimethylthiazolyl) for 2 hours and absorbance was measured at 600 nm. IC₅₀ values were calculated from dose-response curves using GraphPad Prism software.

For the CF-Cis combination treatments, cells were plated in a 96-well plate at 2000 cells per well and treated the next day with either CF, Cis, or CF-Cis combination at the stated ratio. After 48 hours, cells were then incubated with CellTiterGlo Reagent (Promega) according to the manufacturer's protocol. Synergy scores were calculated using either SynergyFinderPlus software or CDI (see the "Statistical analysis" section for details).

Clonogenic assay

Cells were trypsinized, counted, and then resuspended in medium containing CF, Cis, or the stated dose combination of CF and Cis at a density of 1000 cells/ml. One milliliter of cells (1000 cells per well) was plated in one well of a 12-well plate (single-agent studies) or 24-well plate (drug combination studies) for each drug concentration analyzed. Colonies were allowed to form for 7 days and were then stained with crystal violet staining solution [1% (v/v) paraformaldehyde, 10% (v/v) methanol, 0.05% (w/v) crystal violet, in 1× PBS]. Plates were imaged, and staining was quantified using the ColonyArea ImageJ plugin (74). Synergy scores were calculated using SynergyFinderPlus software (see the "Statistical analysis" section for details).

Immunoblotting

Cell pellets were resuspended in 1× radioimmunoprecipitation assay (RIPA) buffer (Millipore, 20-188) containing protease inhibitor (Roche, 11697498001) and phosphatase inhibitor (Roche, 4906845001) cocktail, incubated on ice for 30 min, and then sonicated to lyse cells. Lysates were spun down for 20 min at 12,000 rpm at 4°C, and the supernatant was collected. Protein concentration of lysates was estimated using bicinchoninic acid (BCA) assay (Thermo Fisher Scientific, 23227). Thirty micrograms of sample protein was mixed with sample buffer and then loaded and separated using Criterion XT 4 to 12% bis-tris polyacrylamide gels (Bio-Rad, 3450123) and XT MES Buffer (Bio-Rad, 1610789). Transfer of separated samples from gels to nitrocellulose membranes was performed with the Bio-Rad Trans-Blot Turbo system (Bio-Rad, 1704156). Primary antibodies to BUB1 (Proteintech, 13330-1-AP), E2F1 [Cell Signaling Technology (CST), 3742], Cdc20 (Proteintech, 10252-1-AP), eIF2 α (CST, 9722), eIF4E (CST, 9742), RPS12 (Proteintech, 16490-1-AP), RPS16 (Proteintech, 15603-1-AP), c-MYC (CST, 5605), phospho-4EBP1 (CST, 2855), 4EBP1 (CST, 9644), anti-puromycin (Sigma-Aldrich, MABE343), and vinculin (CST, 13901) were diluted 1:1000 in tris-buffered saline containing 0.1% Tween 20 (TBST) and 5% (w/v) nonfat milk and incubated with membranes overnight at 4°C. Membranes were then washed three times in TBST followed by incubation with horseradish peroxidase (HRP)-conjugated anti-rabbit immunoglobulin G (IgG) antibody (CST, 7074) for 1 hour at room temperature. Western blot images were acquired by chemiluminescence using SuperSignal West Pico Plus (Thermo Fisher Scientific, 34577). Quantification of signal from Western blot bands was performed using ImageLab densitometry software.

Immunohistochemistry

HEYA8 subcutaneous mouse tumors were processed as previously reported (75). Immunohistochemical staining was performed using a 1:500 dilution of antibodies to PAX8 (Novus, NBP1-32440), Ki-67 (CST, 12202), and MYC (CST, 5605). Slides were scanned using a 3D Histech Panoramic Midi scanner. Immunohistochemical staining was quantified using Panoramic SlideViewer software using the densitometry function. For Ki-67 staining, the total number of positive (brown) pixels within nuclei was quantified for the scanned area of the tumor and reported as a percentage of the total area scanned. For MYC staining, the total number of cytoplasmic and nuclear positive (brown) pixels was quantified for the scanned area of the tumor and reported as a percentage of the total area scanned.

Lentiviral transduction

For lentiviral transfection, Lenti Starter Kit (System Biosciences, CA) was used. Briefly, 293T cells (American Type Culture Collection) were transduced with 2 μ g of plasmid and 10 μ g of pPACKH1-plasmid mix with Lipofectamine 2000 (Life Technologies, CA). Forty-eight hours later, virus particles were harvested and precipitated. Target cells were transduced by plating 100,000 cells per well in a six-well plate with virus particles (4 μ g/ml polybrene, Santa Cruz Biotechnology, CA).

Luciferase reporter assay

Cells were plated in six-well plates at 70,000 cells per well. The next day, regular medium was replaced with CF-containing medium and the cells were transfected with the 7× E-box luciferase reporter plasmid (Addgene, plasmid no. 124532). Twenty-four hours after transfection, the cells were lysed and luminescence was measured using

components from the Promega Dual Luciferase Reporter Assay System according to the manufacturer's protocol (Promega, E1910).

MYC siRNA transfection with and without CF treatment

For MYC depletion experiments, HEYA8 or CaOV4 cells were seeded in 2D culture at a density of 40,000 cells per well in 12-well tissue culture plates. After 24 hours, the cells were transfected with either siscram (catalog no. 4390843, Thermo Fisher Scientific), siMYC #1 (assay ID s9129, Thermo Fisher Scientific), or siMYC #2 (assay ID s9131, Thermo Fisher Scientific) according to the manufacturer's instructions. Twenty-four hours after transfection, the transfection medium was removed, and the medium containing either vehicle or CF was added to the appropriate wells. Cells were then incubated for 72 hours in vehicle- or CF-containing medium. After incubation with or without CF, cell viability was assessed via 3-(4,5-dimethylthiazol-2-yl)-2,5-diphenyltetrazolium bromide (MTT) assay. IC₅₀ values were calculated from dose-response curves using GraphPad Prism software. To assess MYC knockdown efficiency, vehicle-treated cells transfected with scrambled siRNA (siscram) or one of two MYC-target siRNAs (siMYC #1 or siMYC #2) were collected 48 hours after transfection and MYC levels were quantified via immunoblotting. Quantification of signal from Western blot bands was performed using ImageLab densitometry software.

Protein synthesis assay

Assay was performed using a modification of the SUNSET assay described in (76). Cells were plated in six-well plates at 100,000 cells per well. The next day, cells were treated with either vehicle or increasing doses of CF for 48 hours, after which the medium from all wells was removed and replaced with the drug-free medium containing puromycin (10 μ g/ml) (Sigma-Aldrich, P8833). Cells were incubated in puromycin medium for 10 min to label nascent polypeptide chains (pulse). Puromycin medium was removed, and all wells were washed once with ice-cold PBS. The puromycin free drug-containing medium was then replaced on cells, and cells were incubated for 50 min at 37°C (chase). Cells were then harvested, and puromycin labeling was measured via Western blotting techniques. As a positive control, cells were also treated with cycloheximide protein synthesis inhibitor (50 μ g/ml) for 24 hours before puromycin pulse/chase in all experiments. Total protein was measured by Ponceau S staining.

Spheroid clearance assay

To measure the ability of HGSOc spheroids to clear a monolayer of OSE cells, HEYA8-RFP or OVCAR8-RFP cells were plated in 2D adherent conditions (six-well plate, 50,000 cells per well). Twenty-four hours after seeding, the HGSOc cells were treated with either vehicle or CF for 48 hours. After drug treatment, the cells were trypsinized and plated into 96-well round-bottom ULA plates in drug-free medium at a density of 500 cells per well. The cells were allowed to form spheroids for 18 to 24 hours. On the same day as sphere formation, HIO-80 GFP cells were seeded into a 96-well plate at a density of 40,000 cells per well to form a confluent monolayer. The HGSOc RFP spheroids were then transferred into the 96-well plate containing HIO-80 GFP cells (one spheroid per well) and allowed to adhere to the monolayer for 24 hours. After 24 hours, the wells containing the monolayer with spheroids were washed with 1× PBS three times to remove any nonattached spheroids. Attached spheroids and monolayer were then imaged using a Nikon Ti2e inverted fluorescence microscope. OSE clearance was calculated by measuring the

GFP-negative area within the circumference of the attached spheroid using NIS Elements image analysis software (Nikon).

Spheroid formation assay

To measure spheroid formation, HEYA8-RFP cells were plated in 2D adherent conditions (six-well plate, 50,000 cells per well). Twenty-four hours after seeding, the cells were treated with either vehicle or CF for 48 hours. After drug treatment, the cells were trypsinized and plated into 96-well round-bottom ULA plates in drug-free medium at a density of 500 cells per well. The cells were allowed to form spheroids for 18 to 24 hours, and then the spheroids were imaged using a Nikon Ti2e inverted fluorescence microscope. The area of each spheroid was measured using NIS Elements image analysis software (Nikon).

Spheroid growth assay

To measure spheroid growth, fluorescently labeled cells were counted and then resuspended in medium containing CF, Cis, or a 1:1 combination of CF and Cis at the appropriate dose at a density of 100 cells per 0.2 ml of medium. Drug + cell medium (0.2 ml) was then added in technical triplicate to the wells of a 96-well round-bottom ULA plate (Corning, 4515). Spheroids were grown for 7 days and then imaged using a Nikon Ti2e inverted fluorescence microscope. Fluorescence intensity was measured for each spheroid using NIS Elements image analysis software (Nikon). Spheroid fluorescence intensity values for biological replicates (average of technical triplicates) were used to generate dose-response curves and IC_{50} values using GraphPad Prism software.

RNA sequencing and IPA

For RNA sequencing, HEYA8 ovarian cancer cells were plated in 10-cm dishes under adherent conditions at a density of 500,000 cells per well. The next day, cells were treated with medium containing CF at concentrations of 0, 1, 5, and 10 μ M for 48 hours. After drug treatment, the cells were collected, and total RNA was extracted from each sample using the Norgen Total RNA Purification Kit (17200). Samples were prepared in collaboration with Children's Hospital of Philadelphia Center for Applied Genomics, and only samples with $OD_{260/280} = 1.9$ to 2.1 and RNA integrity number (RIN) scores >7 were used for sequencing. Samples were prepared using the TrueSeq Total RNA library (RS-122-2001) with ribosomal depletion. Sequencing was performed using an S2 flow cell with 3.3 billion to 4.1 billion read cluster capacity. Bioinformatics analysis was executed using the R package DESeq2 (version 3.16) and performed in collaboration with the Translational Molecular Medicine group at Saint John's Cancer Institute. Significant changes in gene expression were classified as fold change less than/equal to -1.5 or greater than/equal to 1.5 with multiple testing corrected $P \leq 0.01$. IPA (Qiagen) was used to compare samples and identify changes in canonical pathways, diseases and functions, and predicted upstream regulators that occurred in response to treatment with increasing CF dose.

Statistical analysis

Unless otherwise noted, data are presented as the mean \pm SD from three independent experiments. All statistical significance tests were carried out on a single factor (e.g., protein expression) compared between two biological groups (e.g., vehicle versus CF treated). Statistical comparisons of one-factor datasets with only two biological groups were performed using Student's *t* test. Statistical comparisons

of one-factor datasets with three or more biological groups were performed using one-way analysis of variance (ANOVA) with Tukey multiple testing correction unless otherwise stated. $P < 0.05$ was considered statistically significant for both *t* test and one-way ANOVA. To calculate synergy scores for combination dose-response matrices analyzing cell viability, luminescence values for each drug combination were converted to % inhibition using the formula (combination luminescence – vehicle luminescence/vehicle luminescence) $\times -100$. Combination dose-response matrices of % inhibition for $N = 3$ biological replicates were then uploaded into the SynergyFinder software. Synergy scores for each dose combination were calculated using Bliss/Loewe consensus scoring, which combines multiple synergy reference models (Bliss, Loewe, and HSA) with outlier correction turned on (55). Synergy scores for clonogenic combination dose-response matrices were generated using % area values calculated by the ColonyArea ImageJ plugin. % Area values for each drug combination were converted to % inhibition using the formula (combination % Area – vehicle % Area/vehicle % Area) $\times -100$. Synergy scores were then calculated with the SynergyFinder program using the same steps as the cell viability analysis described above. The CDI was calculated for each dose combination using the following formula: $CDI = AB/(A \times B)$, where *AB* is the ratio of the two-drug combination luminescence to the vehicle control luminescence, *A* is the ratio of the single-agent CF luminescence to the vehicle control luminescence, and *B* is the ratio of the single-agent Cis luminescence to the vehicle control luminescence. $CDI < 1$ indicates synergism, $CDI < 0.7$ indicates significant synergism, $CDI = 1$ indicates additivity, and $CD > 1$ indicates antagonism.

Tumor formation assays

All in vivo tumor formation experiments were performed under a protocol reviewed and approved by the Penn Institutional Animal Care and Use Committee (protocol no. 806138). To investigate the effects of CF \pm Cis treatment on in vivo subcutaneous tumor growth, 40 NOD scid gamma (NSG) mice (Jackson Laboratory, strain no. 005557) were each injected subcutaneously with 1,000,000 HEYA8 cells suspended in a 1:1 mixture of DMEM to Matrigel (Corning, 354234) on the lower right flank. Tumors were allowed to grow to 100 mm^3 in size, and then mice were randomized into four treatment groups: (i) vehicle (PBS) treated, (ii) CF treated (1 mg/kg), (iii) Cis treated (1 mg/kg), and (iv) combination treated (0.5 mg/kg CF, 0.5 mg/kg Cis). Each treatment group was dosed three times per week (Monday/Wednesday/Friday) via intratumoral injection for the duration of the study. Tumor volume was measured using calipers every 7 days. All mice were euthanized on day 50 after randomization when the majority (6 of 10) of vehicle-treated mice either had tumors $>2000 mm^3$ or had been euthanized for animal welfare reasons.

For intraperitoneal tumor formation, athymic nude mice were used (Jackson Laboratory, strain no. 007850). All mice were each injected intraperitoneally with 1,000,000 luciferized OVCAR4 cells. Intraperitoneal tumors were allowed to grow to $\geq 1 \times 10^6$ photons per second (p/s) in size, and then mice were randomized into four treatment groups as above for subcutaneous tumor assays. Each treatment group was dosed every 3 days via intraperitoneal injection for the duration of the study. Tumor volume was measured using bioluminescence imaging every 7 days. All mice were euthanized for animal welfare reasons as they became moribund with tumor burden.

Supplementary Materials

The PDF file includes:

Figs. S1 to S9

Table S1

Other Supplementary Material for this manuscript includes the following:

MDAR Reproducibility Checklist

REFERENCES AND NOTES

- International Agency for Research on Cancer, Cancer tomorrow; https://gco.iarc.fr/tomorrow/en/dataviz/trends?types=0_1&sexes=2&mode=population&group_populations=0&multiple_populations=1&multiple_cancers=0&cancers=25&populations=900.
- A. M. Karst, R. Drapkin, Ovarian cancer pathogenesis: A model in evolution. *J. Oncol.* **2010**, 932371 (2010).
- S. Lheureux, C. Gourley, I. Vergote, A. M. Oza, Epithelial ovarian cancer. *Lancet* **393**, 1240–1253 (2019).
- L. A. Torre, B. Trabert, C. DeSantis, K. D. Miller, G. Samimi, C. D. Runowicz, M. M. Gaudet, A. Jemal, R. L. Siegel, Ovarian cancer statistics, 2018. *CA Cancer J. Clin.* **68**, 284–296 (2018).
- C. Aghajanian, B. Goff, L. R. Nycum, Y. V. Wang, A. Husain, S. V. Blank, Final overall survival and safety analysis of OCEANS, a phase 3 trial of chemotherapy with or without bevacizumab in patients with platinum-sensitive recurrent ovarian cancer. *Gynecol. Oncol.* **139**, 10–16 (2015).
- T. J. Perren, A. M. Swart, J. Pfisterer, J. A. Ledermann, E. Pujade-Lauraine, G. Kristensen, M. S. Carey, P. Beale, A. Cervantes, C. Kurzeder, A. Bois, J. Sehouli, R. Kimmig, A. Stähle, F. Collinson, S. Essapen, C. Gourley, A. Lortholary, F. Selle, M. R. Mirza, A. Leminen, M. Plante, D. Stark, W. Qian, M. K. B. Parmar, A. M. Oza, A phase 3 trial of bevacizumab in ovarian cancer. *N. Engl. J. Med.* **365**, 2484–2496 (2011).
- R. A. Burger, M. F. Brady, M. A. Bookman, G. F. Fleming, B. J. Monk, H. Huang, R. S. Mannel, H. D. Homesley, J. Fowler, B. E. Greer, M. Boente, M. J. Birrer, S. X. Liang, Incorporation of bevacizumab in the primary treatment of ovarian cancer. *N. Engl. J. Med.* **365**, 2473–2483 (2011).
- K. N. Maxwell, S. M. Domchek, Cancer treatment according to BRCA1 and BRCA2 mutations. *Nat. Rev. Clin. Oncol.* **9**, 520–528 (2012).
- M. R. Mirza, R. L. Coleman, A. González-Martín, K. N. Moore, N. Colombo, I. Ray-Coquard, S. Pignata, The forefront of ovarian cancer therapy: Update on PARP inhibitors. *Ann. Oncol.* **31**, 1148–1159 (2020).
- K. C. Kurnit, M. Avila, E. M. Hinchcliff, R. L. Coleman, S. N. Westin, PARP inhibition in the ovarian cancer patient: Current approvals and future directions. *Pharmacol. Ther.* **213**, 107588 (2020).
- L. Rossi, M. Verrico, E. Zaccarelli, A. Papa, M. Colonna, M. Strudel, P. Vici, V. Bianco, F. Tomao, Bevacizumab in ovarian cancer: A critical review of phase III studies. *Oncotarget* **8**, 12389–12405 (2017).
- K. S. Tewari, R. A. Burger, D. Enserro, B. M. Norquist, E. M. Swisher, M. F. Brady, M. A. Bookman, G. F. Fleming, H. Huang, H. D. Homesley, J. M. Fowler, B. E. Greer, M. Boente, S. X. Liang, C. Ye, C. Bais, L. M. Randall, J. K. Chan, J. S. Ferriss, R. L. Coleman, C. Aghajanian, T. J. Herzog, P. J. DiSaia, L. J. Copeland, R. S. Mannel, M. J. Birrer, B. J. Monk, Final overall survival of a randomized trial of bevacizumab for primary treatment of ovarian cancer. *J. Clin. Oncol.* **37**, 2317–2328 (2019).
- L. Sapio, M. Gallo, M. Illiano, E. Chiosi, D. Naviglio, A. Spina, S. Naviglio, The natural cAMP elevating compound forskolin in cancer therapy: Is it time? *J. Cell. Physiol.* **232**, 922–927 (2017).
- S. V. Bhat, B. S. Bajqwa, H. Dornauer, N. J. do Scusa, H. W. Fehlhaber, Structures and stereochemistry of new labdane diterpenoids from *Coleus forskohlii* Briq. *Tetrahedron Lett.* **18**, 1669–1672 (1977).
- C. Kavitha, K. Rajamani, E. Vadivel, *Coleus forskohlii*—A comprehensive review on morphology, phytochemistry and pharmacological aspects. *J. Med. Plant Res.* **4**, 278–285 (2010).
- K. B. Seamon, W. Padgett, J. W. Daly, Forskolin: Unique diterpene activator of adenylate cyclase in membranes and in intact cells. *Proc. Natl. Acad. Sci. U.S.A.* **78**, 3363–3367 (1981).
- C. Pinto, D. Papa, M. Hübner, T. C. Mou, G. H. Lushington, R. Seifert, Activation and inhibition of adenylate cyclase isoforms by forskolin analogs. *J. Pharmacol. Exp. Ther.* **325**, 27–36 (2008).
- A. Laurenza, E. M. H. Sutkowski, K. B. Seamon, Forskolin: A specific stimulator of adenylate cyclase or a diterpene with multiple sites of action? *Trends Pharmacol. Sci.* **10**, 442–447 (1989).
- P. Sassone-Corsi, The cyclic AMP pathway. *Cold Spring Harb. Perspect. Biol.* **4**, a011148 (2012).
- K. Yan, L.-N. Gao, Y.-L. Cui, Y. Zhang, X. Zhou, The cyclic AMP signaling pathway: Exploring targets for successful drug discovery (review). *Mol. Med. Rep.* **13**, 3715–3723 (2016).
- A. Kilanowska, A. Ziolkowska, P. Stasiak, M. Gibas-Dorna, cAMP-dependent signaling and ovarian cancer. *Cells* **11**, 3835 (2022).
- M. Piontek, K. J. Hengels, R. Porschen, G. Strohmeyer, Protein kinase C and adenylate cyclase as targets for growth inhibition of human gastric cancer cells. *J. Cancer Res. Clin. Oncol.* **119**, 697–699 (1993).
- K. B. Gützkow, S. Naderi, H. K. Blomhoff, Forskolin-mediated G1 arrest in acute lymphoblastic leukaemia cells: Phosphorylated pRB sequesters E2Fs. *J. Cell Sci.* **115**, 1073–1082 (2002).
- D. G. McEwan, V. G. Brunton, G. S. Baillie, N. R. Leslie, M. D. Houslay, M. C. Frame, Chemoresistant KM12C colon cancer cells are addicted to low cyclic AMP levels in a phosphodiesterase 4–regulated compartment via effects on phosphoinositide 3-kinase. *Cancer Res.* **67**, 5248–5257 (2007).
- K. C. Agarwal, R. E. Parks Jr., Forskolin: A potential antimetastatic agent. *Int. J. Cancer* **32**, 801–804 (1983).
- A. Burduga, A. Conant, L. Haynes, J. Zhang, K. Jalink, R. Sutton, J. Neoptolemos, E. Costello, A. Tepik, cAMP inhibits migration, ruffling and paxillin accumulation in focal adhesions of pancreatic ductal adenocarcinoma cells: Effects of PKA and EPAC. *Biochim. Biophys. Acta* **1833**, 2664–2672 (2013).
- Y. Ou, X. Zheng, Y. Gao, M. Shu, T. Leng, Y. Li, W. Yin, W. Zhu, Y. Huang, Y. Zhou, J. Tang, P. Qiu, G. Yan, J. Hu, H. Ruan, H. Hu, Activation of cyclic AMP/PKA pathway inhibits bladder cancer cell invasion by targeting MAP4-dependent microtubule dynamics. *Urol. Oncol.* **32**, 47.e21–47.e28 (2014).
- H. Dong, K. P. Claffey, S. Brocke, P. M. Epstein, Inhibition of breast cancer cell migration by activation of cAMP signaling. *Breast Cancer Res. Treat.* **152**, 17–28 (2015).
- D. R. Pattabiraman, B. Bierie, K. I. Kober, P. Thiru, J. A. Krall, C. Zill, F. Reinhardt, W. L. Tam, R. A. Weinberg, Activation of PKA leads to mesenchymal-to-epithelial transition and loss of tumor-initiating ability. *Science* **351**, aad3680 (2016).
- S. C. Mann, P. A. Andrews, S. B. Howell, Modulation of cis-diamminedichloroplatinum(II) accumulation and sensitivity by forskolin and 3-isobutyl-1-methylxanthine in sensitive and resistant human ovarian carcinoma cells. *Int. J. Cancer* **48**, 866–872 (1991).
- S. W. Warrenfeltz, S. A. Lott, T. M. Palmer, J. C. Gray, D. Puett, Luteinizing hormone-induced up-regulation of ErbB-2 is insufficient stimulant of growth and invasion in ovarian cancer cells. *Mol. Cancer Res.* **6**, 1775–1785 (2008).
- T. D'Souza, R. Agarwal, P. J. Morin, Phosphorylation of claudin-3 at threonine 192 by cAMP-dependent protein kinase regulates tight junction barrier function in ovarian cancer cells. *J. Biol. Chem.* **280**, 26233–26240 (2005).
- M. Kamrava, F. Simpkins, E. Alejandro, C. Michener, E. Meltzer, E. C. Kohn, Lysophosphatidic acid and endothelin-induced proliferation of ovarian cancer cell lines is mitigated by neutralization of granulins—epithelin precursor (GEP), a prosurvival factor for ovarian cancer. *Oncogene* **24**, 7084–7093 (2005).
- A. Takahashi, K. Kato, A. Kuboyama, T. Inoue, Y. Tanaka, A. Kuhara, K. Kinoshita, S. Takeda, N. Wake, Induction of senescence by progesterone receptor-B activation in response to cAMP in ovarian cancer cells. *Gynecol. Oncol.* **113**, 270–276 (2009).
- T. J. Shaw, E. J. Kesztelyi, A. M. Tonary, M. Cada, B. C. Vanderhyden, Cyclic AMP in ovarian cancer cells both inhibits proliferation and increases c-KIT expression. *Exp. Cell Res.* **273**, 95–106 (2002).
- S. Gong, Y. Chen, F. Meng, Y. Zhang, C. Li, G. Zhang, W. Huan, F. Wu, Roflumilast enhances cisplatin-sensitivity and reverses cisplatin-resistance of ovarian cancer cells via cAMP/PKA/CREB-FtMt signalling axis. *Cell Prolif.* **51**, e12474 (2018).
- A. Mistarz, M. Graczyk, M. Winkler, P. K. Singh, E. Cortes, A. Miliotto, S. Liu, M. Long, L. Yan, A. Stablewski, K. O'Loughlin, H. Minderman, K. Odunsi, H. Rokita, A. J. R. McGray, E. Zsiros, D. Kozbor, Induction of cell death in ovarian cancer cells by doxorubicin and oncolytic vaccinia virus is associated with CREB3L1 activation. *Mol. Ther. Oncolytics* **23**, 38–50 (2021).
- P. Zhu, L. Wang, P. Xu, Q. Tan, Y. Wang, G. Feng, L. Yuan, GANT61 elevates chemosensitivity to cisplatin through regulating the Hedgehog, AMPK and cAMP pathways in ovarian cancer. *Future Med. Chem.* **14**, 479–500 (2022).
- N. Dimitrova, A. B. Nagaraj, A. Razi, S. Singh, S. Kamalakaran, N. Banerjee, P. Joseph, A. Mankovich, P. Mittal, A. DiFeo, V. Varadan, InFlo: A novel systems biology framework identifies cAMP-CREB1 axis as a key modulator of platinum resistance in ovarian cancer. *Oncogene* **36**, 2472–2482 (2016).
- L. Tong, Y. Wang, Y. Ao, X. Sun, CREB1 induced lncRNA HAS2-AS1 promotes epithelial ovarian cancer proliferation and invasion via the miR-466/RUNX2 axis. *Biomed. Pharmacother.* **115**, 108891 (2019).
- M. P. Godard, B. A. Johnson, S. R. Richmond, Body composition and hormonal adaptations associated with forskolin consumption in overweight and obese men. *Obes. Res.* **13**, 1335–1343 (2005).
- The effect of *Coleus forskohlii* extract on the risk factors of metabolic syndrome (clinicaltrials.gov, 2014); <https://clinicaltrials.gov/ct2/show/NCT02143349>.
- R. González-Sánchez, X. Trujillo, B. Trujillo-Hernández, C. Vásquez, M. Huerta, A. Elizalde, Forskolin versus sodium cromoglycate for prevention of asthma attacks: A single-blinded clinical trial. *Int. J. Med. Res.* **34**, 200–207 (2006).
- K. Bauer, F. Dietersdorfer, K. Sertl, B. Kaik, G. Kaik, Pharmacodynamic effects of inhaled dry powder formulations of fenoterol and colforsin in asthma. *Clin. Pharmacol. Ther.* **53**, 76–83 (1993).

45. V. D. Wagh, P. N. Patil, S. J. Surana, K. V. Wagh, Forskolin: Upcoming antiglaucoma molecule. *J. Postgrad. Med.* **58**, 199–202 (2012).
46. Retinal nerve fibres layers thickness study in glaucomatous patients (clinicaltrials.gov, 2010); <https://clinicaltrials.gov/ct2/show/study/NCT01254006>.
47. Y. Khandelwal, K. Rajeshwari, R. Rajagopalan, L. Swamy, A. N. Dohadwalla, N. J. De Souza, R. H. Rupp, Cardiovascular effects of new water-soluble derivatives of forskolin. *J. Med. Chem.* **31**, 1872–1879 (1988).
48. S. Suzuki, O. Ito, T. Sayama, K. Goto, Intra-arterial colforsin daropate for the treatment of cerebral vasospasm after aneurysmal subarachnoid hemorrhage. *Neuroradiology* **52**, 837–845 (2010).
49. N. Hayashida, S. Chihara, E. Tayama, T. Takaseya, N. Enomoto, T. Kawara, S. Aoyagi, Antiinflammatory effects of colforsin daropate hydrochloride, a novel water-soluble forskolin derivative. *Ann. Thorac. Surg.* **71**, 1931–1938 (2001).
50. M. Kikura, K. Morita, S. Sato, Pharmacokinetics and a simulation model of colforsin daropate, new forskolin derivative inotropic vasodilator, in patients undergoing coronary artery bypass grafting. *Pharmacol. Res.* **49**, 275–281 (2004).
51. A. B. Nagaraj, P. Joseph, O. Kovalenko, S. Singh, A. Armstrong, R. Redline, K. Resnick, K. Zanotti, S. Waggoner, A. DiFeo, Critical role of Wnt/ β -catenin signaling in driving epithelial ovarian cancer platinum resistance. *Oncotarget* **6**, 23720–23734 (2015).
52. C. Yee, K.-A. Dickson, M. N. Muntasar, Y. Ma, D. J. Marsh, Three-dimensional modelling of ovarian cancer: From cell lines to organoids for discovery and personalized medicine. *Front. Bioeng. Biotechnol.* **10**, 836984 (2022).
53. K. Shield, M. L. Ackland, N. Ahmed, G. E. Rice, Multicellular spheroids in ovarian cancer metastases: Biology and pathology. *Gynecol. Oncol.* **113**, 143–148 (2009).
54. M. P. Iwanicki, H.-Y. Chen, C. Iavarone, I. K. Zervantonakis, T. Muranen, M. Novak, T. A. Ince, R. Drapkin, J. S. Brugge, Mutant p53 regulates ovarian cancer transformed phenotypes through autocrine matrix deposition. *JCI Insight* **1**, e86829 (2016).
55. A. Ianevski, A. K. Giri, T. Aittokallio, SynergyFinder 3.0: An interactive analysis and consensus interpretation of multi-drug synergies across multiple samples. *Nucleic Acids Res.* **50**, W739–W743 (2022).
56. H. Kim, E. George, R. Ragland, S. Rafail, R. Zhang, C. Krepler, M. Morgan, M. Herlyn, E. Brown, F. Simpkins, Targeting the ATR/CHK1 axis with PARP inhibition results in tumor regression in BRCA-mutant ovarian cancer models. *Clin. Cancer Res.* **23**, 3097–3108 (2017).
57. L. Huang, J. Wang, B. Fang, F. Meric-Bernstam, J. A. Roth, M. J. Ha, CombPDX: A unified statistical framework for evaluating drug synergism in patient-derived xenografts. *Sci. Rep.* **12**, 12984 (2022).
58. P. Hao, J. Yu, R. Ward, Y. Liu, Q. Hao, S. An, T. Xu, Eukaryotic translation initiation factors as promising targets in cancer therapy. *Cell Commun. Signal.* **18**, 175 (2020).
59. J. M. Reyes-González, P. E. Vivas-Mejía, c-MYC and epithelial ovarian cancer. *Front. Oncol.* **11**, 601512 (2021).
60. J. Musa, M. F. Orth, M. Dallmayer, M. Baldauf, C. Pardo, B. Rotblat, T. Kirchner, G. Leprivier, T. G. P. Grünwald, Eukaryotic initiation factor 4E-binding protein 1 (4E-BP1): A master regulator of mRNA translation involved in tumorigenesis. *Oncogene* **35**, 4675–4688 (2016).
61. A. Elia, R. Henry-Grant, C. Adiseshiah, C. Marboeuf, R. J. Buckley, M. J. Clemens, S. Mudan, S. Pyronnet, Implication of 4E-BP1 protein dephosphorylation and accumulation in pancreatic cancer cell death induced by combined gemcitabine and TRAIL. *Cell Death Dis.* **8**, 3204 (2017).
62. Y. Wang, J. Lei, S. Zhang, X. Wang, J. Jin, Y. Liu, M. Gan, Y. Yuan, L. Sun, X. Li, T. Han, J.-B. Wang, 4EBP1 senses extracellular glucose deprivation and initiates cell death signaling in lung cancer. *Cell Death Dis.* **13**, 1075 (2022).
63. D. C. Fingar, C. J. Richardson, A. R. Tee, L. Cheatham, C. Tsou, J. Blenis, mTOR controls cell cycle progression through its cell growth effectors S6K1 and 4E-BP1/eukaryotic translation initiation factor 4E. *Mol. Cell Biol.* **24**, 200–216 (2004).
64. M. Pourdehnad, M. L. Truitt, I. N. Siddiqi, G. S. Ducker, K. M. Shokat, D. Ruggero, Myc and mTOR converge on a common node in protein synthesis control that confers synthetic lethality in Myc-driven cancers. *Proc. Natl. Acad. Sci. U.S.A.* **110**, 11988–11993 (2013).
65. S. Makhija, D. D. Taylor, R. K. Gibb, C. Gerçel-Taylor, Taxol-induced Bcl-2 phosphorylation in ovarian cancer cell monolayer and spheroids. *Int. J. Oncol.* **14**, 515–521 (1999).
66. S. L'Espérance, M. Bachvarova, B. Tetu, A.-M. Mes-Masson, D. Bachvarov, Global gene expression analysis of early response to chemotherapy treatment in ovarian cancer spheroids. *BMC Genomics* **9**, 99 (2008).
67. Z. Turi, M. Lacey, M. Mistrik, P. Moudry, Impaired ribosome biogenesis: Mechanisms and relevance to cancer and aging. *Aging* **11**, 2512–2540 (2019).
68. A. Stedman, S. Beck-Cormier, M. Le Bouteiller, A. Raveux, S. Vandormael-Pourmin, S. Coqueran, V. Lejour, L. Jarzebowski, F. Toledo, S. Robine, M. Cohen-Tannoudji, Ribosome biogenesis dysfunction leads to p53-mediated apoptosis and goblet cell differentiation of mouse intestinal stem/progenitor cells. *Cell Death Differ.* **22**, 1865–1876 (2015).
69. F. W. Chen, Y. A. Ioannou, Ribosomal proteins in cell proliferation and apoptosis. *Int. Rev. Immunol.* **18**, 429–448 (1999).
70. M. S. Lindström, J. Bartek, A. Maya-Mendoza, p53 at the crossroad of DNA replication and ribosome biogenesis stress pathways. *Cell Death Differ.* **29**, 972–982 (2022).
71. F. Lessard, S. Igelmann, C. Trahan, G. Huot, E. Saint-Germain, L. Mignacca, N. D. Toro, S. Lopes-Paciencia, B. L. Calvé, M. Montero, X. Deschênes-Simard, M. Bury, O. Moiseeva, M.-C. Rowell, C. E. Zorca, D. Zenklusen, L. Brakier-Gingras, V. Bourdeau, M. Oeffinger, G. Ferbeyre, Senescence-associated ribosome biogenesis defects contributes to cell cycle arrest through the Rb pathway. *Nat. Cell Biol.* **20**, 789–799 (2018).
72. V. Lombart, M. R. Mansour, Therapeutic targeting of “undruggable” MYC. *EBioMedicine* **75**, 103756 (2022).
73. M. Zeng, N. P. Kwiatkowski, T. Zhang, B. Nabet, M. Xu, Y. Liang, C. Quan, J. Wang, M. Hao, S. Palakurthi, S. Zhou, Q. Zeng, P. T. Kirschmeier, K. Meghani, A. L. Leggett, J. Qi, G. I. Shapiro, J. F. Liu, U. A. Matulonis, C. Y. Lin, P. A. Konstantinopoulos, N. S. Gray, Targeting MYC dependency in ovarian cancer through inhibition of CDK7 and CDK12/13. *eLife* **7**, e39030 (2018).
74. C. Guzmán, M. Bagga, A. Kaur, J. Westermarck, D. Abankwa, ColonyArea: An imageJ plugin to automatically quantify colony formation in clonogenic assays. *PLOS ONE* **9**, e92444 (2014).
75. J. Hooda, M. Novak, M. P. Salomon, C. Matsuba, R. I. Ramos, E. M. Duffie, M. Song, M. S. Hirsch, J. Lester, V. Parkash, B. Y. Karlan, M. Oren, D. S. Hoon, R. Drapkin, Early loss of histone H2B monoubiquitylation alters chromatin accessibility and activates key immune pathways that facilitate progression of ovarian cancer. *Cancer Res.* **79**, 760–772 (2019).
76. E. K. Schmidt, G. Clavarino, M. Ceppi, P. Pierre, SUNSET, a nonradioactive method to monitor protein synthesis. *Nat. Methods* **6**, 275–277 (2009).

Acknowledgements: We thank J. Salvino and C. Eischen for critical review of the manuscript. We thank the Saint John's Cancer Institute sequencing center for providing RNA sequencing services. We thank M. Zheng for assistance with histology. **Funding:** This study was supported by the National Institutes of Health P50 SPORE CA228991 (R.D.), the Department of Defense W81XWH-21-1-0643 (M.J.K.) and W81XWH-22-1-0852 (R.D.), the Dr. Miriam and Sheldon G. Adelson Medical Research Foundation (R.D. and D.S.B.H.), the Honorable Tina Brozman Foundation for Ovarian Cancer Research (R.D.), the Claneil Foundation (R.D.), the Gray Foundation (R.D.), the Carl H. Goldsmith Ovarian Cancer Translational Research Fund (R.D.), the Marjorie S. Stanek and Lowell H. Dubrow Ovarian Cancer Research Center Endowed Fund (R.D.), the Mike and Patti Hennessy Foundation (R.D.), the Monica K. Young Foundation (R.D.), Susan and David Wolk (R.D.), and the Basser Center for BRCA (M.J.K. and R.D.). **Author contributions:** This project was conceived and designed by M.J.K. and R.D. M.J.K. conducted experiments and acquired/analyzed all subsequent data. RNA sequencing analysis was conducted by P.R., J.M., and D.S.B.H. HGSOX PDX cell lines were provided by A.D. M.J.K. and R.D. wrote and revised the manuscript. All authors reviewed and approved the manuscript before submission. **Competing interests:** R.D. serves on the scientific advisory board of VOC Health and Repare Therapeutics. The other authors declare that they have no competing interests. **Data and materials availability:** The RNA-sequencing dataset (GSE) has been deposited in GEO, accession ID GSE280516. All other data needed to evaluate the conclusions in the paper are present in the paper or the Supplementary Materials.

Submitted 22 February 2024
Accepted 30 October 2024
Published 19 November 2024
10.1126/scisignal.ado8303